



GONG Catalog of Solar Filament Oscillations Near Solar Maximum

M. Luna^{1,2} , J. Karpen³ , J. L. Ballester^{4,5} , K. Muglach^{3,6}, J. Terradas^{4,5} , T. Kucera³ , and H. Gilbert³

¹Instituto de Astrofísica de Canarias, E-38200 La Laguna, Tenerife, Spain

²Departamento de Astrofísica, Universidad de La Laguna, E-38206 La Laguna, Tenerife, Spain

³NASA Goddard Space Flight Center, Greenbelt, MD 20771, USA

⁴Departament de Física, Universitat de les Illes Balears (UIB), E-07122 Palma de Mallorca, Spain

⁵Institute of Applied Computing & Community Code (IAC³), UIB, Spain

⁶Catholic University of America, Washington, DC 20064, USA

Received 2018 March 9; revised 2018 April 6; accepted 2018 April 10; published 2018 May 30

Abstract

We have cataloged 196 filament oscillations from the Global Oscillation Network Group H α network data during several months near the maximum of solar cycle 24 (2014 January–June). Selected examples from the catalog are described in detail, along with our statistical analyses of all events. Oscillations were classified according to their velocity amplitude: 106 small-amplitude oscillations (SAOs), with velocities $<10 \text{ km s}^{-1}$, and 90 large-amplitude oscillations (LAOs), with velocities $>10 \text{ km s}^{-1}$. Both SAOs and LAOs are common, with one event of each class every two days on the visible side of the Sun. For nearly half of the events, we identified their apparent trigger. The period distribution has a mean value of 58 ± 15 minutes for both types of oscillations. The distribution of the damping time per period peaks at $\tau/P = 1.75$ and 1.25 for SAOs and LAOs, respectively. We confirmed that LAO damping rates depend nonlinearly on the oscillation velocity. The angle between the direction of motion and the filament spine has a distribution centered at 27° for all filament types. This angle agrees with the observed direction of filament-channel magnetic fields, indicating that most of the cataloged events are longitudinal (i.e., undergo field-aligned motions). We applied seismology to determine the average radius of curvature in the magnetic dipoles, $R \approx 89 \text{ Mm}$, and the average minimum magnetic field strength, $B \approx 16 \text{ G}$. The catalog is available to the community online and is intended to be expanded to cover at least 1 solar cycle.

Key words: catalogs – Sun: filaments, prominences – Sun: magnetic fields – Sun: oscillations

1. Introduction

Filament oscillations were first observed visually (Greaves, Newton, & Jackson, reported by Dyson 1930; Newton 1935; Bruzek 1951), followed by photographic observations that revealed a significant relationship with flares (Dodson 1949; Bruzek & Becker 1957 and Becker 1958). Moreton & Ramsey (1960) confirmed that wave disturbances initiated during the impulsive phase of flares were responsible for triggering prominence oscillations both near to and far from the flare. Ramsey & Smith (1966) determined periods and damping times for several oscillating filaments, but did not find any correlation between the period or damping time and the dimensions of the filament, the distance to the associated flare, or its size. In these early observations, some events were called “winking filaments” because these filaments were visible in H α when they were at rest, but disappeared while oscillating. Because these observations were made with narrow-band H α filters, Doppler-shifted absorption from prominence material traveling at sufficiently large line-of-sight (LOS) velocities ($>23 \text{ km s}^{-1}$) fell outside the 0.5 \AA bandpass of the filter and thus became invisible in H α .

Nowadays, thanks to both space- and ground-based instruments, observations of large-amplitude filament oscillations (LAOs: $v > 10 \text{ km s}^{-1}$) have become common. (The terms “large” and “small” amplitude are defined later in this section). The excitors identified thus far include Moreton or EIT waves (Eto et al. 2002; Okamoto et al. 2004; Gilbert et al. 2008; Asai et al. 2012), EUV waves (Liu et al. 2012; Shen et al. 2014a; Xue et al. 2014; Takahashi et al. 2015), shock waves (Shen et al. 2014b), nearby jets, subflares and flares (Jing et al. 2003, 2006; Vrřnak et al. 2007; Li & Zhang 2012), and the

eruption of the filament (Isobe & Tripathi 2006; Isobe et al. 2007; Pouget 2007; Chen et al. 2008; Foullon et al. 2009; Bocchialini et al. 2011).

Many of the observed flare-induced LAOs in filaments exhibit motions in different directions relative to the axial magnetic field (polarization). For instance, the material can undergo vertical (Eto et al. 2002; Okamoto et al. 2004; Shen et al. 2014a), horizontal (Kleczeck & Kuperus 1969; Hershaw et al. 2011; Gosain & Foullon 2012; Liu et al. 2012; Shen et al. 2014b), or longitudinal (field-aligned; Jing et al. 2003, 2006; Vrřnak et al. 2007; Li & Zhang 2012; Zhang et al. 2012; Luna et al. 2014; Shen et al. 2014b) motions. Oscillations with a mixed character (Gilbert et al. 2008) have also been observed.

The first theoretical models proposed to explain the excitation, restoring forces, and damping mechanisms of large-amplitude longitudinal oscillations (LALOs) were purely analytical (Hyder 1966; Kleczeck & Kuperus 1969). One-dimensional, hydrodynamic, numerical models have been employed successfully to describe longitudinal oscillations (Vrřnak et al. 2007; Luna & Karpen 2012; Luna et al. 2012; Zhang et al. 2012, 2013; Ruderman & Luna 2016; Zhou et al. 2017), while 2D and 3D MHD models have described more completely the features of observed longitudinal and transverse oscillations (Terradas et al. 2013, 2015, 2016; Luna et al. 2016).

Spectroscopic techniques have revealed oscillations with much smaller peak velocities than those of LAOs, with amplitudes from the noise level of $0.1\text{--}10 \text{ km s}^{-1}$. Harvey (1969) first measured oscillatory periods between 1 and 17 minutes, while later observations yielded characteristic periods ranging from a few to 90 minutes. Although the triggering mechanisms of these small-amplitude oscillations (SAOs) have

not been clearly identified, they are generally believed to be excited by the periodic motions of filament magnetic fields driven by photospheric or chromospheric oscillations (see the review by Arregui et al. 2012).

A variety of approaches has been used to categorize and understand filament oscillations. The simplest are based on a single property, such as the peak velocity (e.g., Arregui et al. 2012), the nature of the trigger (e.g., Oliver 1999; Oliver & Ballester 2002), or the period (e.g., Arregui et al. 2012). The apparent tendency of periods to group below 10 minutes, in the range of 10–40 minutes, or in the range of 40–90 minutes (Arregui et al. 2012) led to classifications denoted as short-, intermediate-, and long-period oscillations, respectively. Very short periods below 1 minute (Balthasar et al. 1993), very long periods above 5 hr (Foullon et al. 2004; Pouget et al. 2006), and even periods longer than 20 hr (Efremov et al. 2016) have been reported. Classification based only on the period does not reflect the nature, origin, or exciter of the oscillations, however. More complex schemes have proven to be difficult to employ consistently (e.g., Vrřnak 1993).

Because oscillation velocities have been measured from the observable threshold to 100 km s^{-1} , the velocity amplitude alone is not the most definitive criterion by which oscillation events can be categorized. In spite of these limitations, a widely accepted, velocity-based division between small-amplitude and large-amplitude oscillations has proven to be both convenient and physically justifiable. We can relate the observed oscillation amplitudes to their linear or nonlinear character by considering the characteristic Alfvén and sound speeds in prominences, which are of the order of 100 km s^{-1} and 10 km s^{-1} , respectively. Therefore, oscillations with velocity amplitudes above 10 km s^{-1} exceed the local sound speed, and hence can be considered nonlinear oscillations, while smaller velocity amplitudes would be linear. In general, SAOs exhibit amplitudes below 10 km s^{-1} , are not related to flare activity, are local, and can be appropriately analyzed or modeled using methods of linear perturbations. LAOs are usually associated with energetic events, are of global character, and as the velocity amplitude is $\geq 10\text{--}20 \text{ km s}^{-1}$, require a nonlinear approach. As we demonstrate in the present work, however, exceptions to these “rules” exist.

Prominence seismology aims to determine physical parameters that are difficult to measure by direct means in these magnetized plasma structures. This remote diagnostics method combines observations of oscillations and waves in these structures with theoretical results from the analysis of oscillatory properties of given prominence models, as first suggested by Tandberg-Hanssen (1995). The first seismological determinations of magnetic field strength in winking filaments used a simple model of longitudinal motions based on a harmonic oscillator (Hyder 1966; Kleczek & Kuperus 1969). Vrřnak et al. (2007) analyzed LALOs in a prominence to infer the Alfvén speed; assuming the mass density of the prominence plasma, they also determined the azimuthal and axial magnetic field strengths. Our theoretical investigation of oscillations in simulated prominence threads strengthened the foundations of the damped harmonic oscillator model for LALOs, providing a basis for applications to observations (Luna & Karpen 2012; Luna et al. 2012). Subsequent seismological analyses of LALOs in prominences have derived the radius of curvature of dipped field lines supporting prominence threads, the minimum magnetic field strength,

the energy injected by the triggering jet, and the mass accretion rate according to the thermal nonequilibrium model (Li & Zhang 2012; Bi et al. 2014; Luna et al. 2014, 2016; Zhang et al. 2017b). Using the same seismological techniques, we determined the curvature radius of the magnetic field dips and the minimum field strength from the largest prominence oscillation ever reported in the literature; these results were validated by reconstructing the filament magnetic field from the photospheric field in combination with the flux-rope insertion method (Luna et al. 2017).

To interpret observed prominence LAOs directed transverse to the magnetic field, an MHD approach is required. Some observations of oscillatory behavior have been interpreted and analyzed as global or standing kink modes (e.g., Hershaw et al. 2011; Liu et al. 2012; Xue et al. 2014). A theoretical analysis predicted a linear relationship between the damping time (τ) and the period (P) that could be compatible with resonant absorption as the damping mechanism (Ofman & Aschwanden 2002; Ruderman & Roberts 2002; Arregui et al. 2008b). However, this interpretation must be considered with care because the use of scaling laws to discriminate between damping mechanisms is questionable, at least for resonant absorption (Arregui et al. 2008a). Much work remains before the physical models of both longitudinal and transverse LAOs are sufficiently detailed and comprehensive to adequately link theory and simulations with observed prominence motions.

To date, all studies of oscillating prominences have been focused on one or, at most, a few episodes. In order to understand this phenomenon thoroughly and derive key physical characteristics via seismology of all types of prominences over the solar cycle, we have begun to compile a systematic, large data set of oscillation events. Thus far we have identified and analyzed 196 events during several months close to the maximum of solar cycle 24, using Global Oscillation Network Group (GONG) $H\alpha$ data. We found that LAOs are very common on the Sun (one event every 2 days on the visible hemisphere), and that the frequency of SAOs is similar to that of LAOs, yielding one SAO or LAO per day. Our large sample of prominence oscillations has enabled the first statistically significant study of filament oscillations and their pertinent properties, including their apparent triggers, damping times, periods, filament type, filament dimensions, peak velocities, directionality with respect to the filament spine, and maximum displacements. With the information in this catalog, one can derive minimum field strength and other unobservable characteristics through seismology, and begin to explore the implications of longitudinal and transverse oscillations for prominence stability, evolution, and eruption. We have made the catalog available to the community at the following URL: <http://www.iac.es/galeria/mluna/pages/gong-catalogue-of-laos.php>.

This paper presents both individual examples of interest and statistical analyses that explore potential relationships among the derived parameters. In Section 2 the GONG data used in the catalog are described, while in Section 3 the GONG catalog of prominence oscillations is introduced. Section 4 presents the method used to detect oscillations and select events for the catalog. The criteria used to classify prominence types are introduced in Section 5. Section 6 explains how we identified the triggering mechanism and derived the filament parameters. Sections 7 and 8 discuss the time–distance approach and analysis methods used to characterize the oscillations, respectively.

Section 9 describes selected events in detail, while in Section 10 we present the results of our statistical study of filament oscillations. A seismological analysis of selected events is included in Section 11, and the results are summarized in Section 12. We describe our new method for constructing time–distance diagrams with data from curved slits in the [Appendix](#).

2. Description of the NSO GONG Network Data

Nowadays it is possible to monitor the full Sun nearly continuously with the space-based *Solar Dynamics Observatory* (*SDO*; Lemen et al. 2012) or the ground-based network of telescopes of the GONG (<http://gong2.nso.edu>). Continuous coverage of the full Sun is needed for a complete study of filament oscillation events. *SDO* offers the best spatial resolution and temporal cadence, and the observations are independent of the local conditions of the Earth’s atmosphere, in contrast to the GONG telescopes. However, the filaments and their periodic movements are not easy to detect in *SDO* data. In some situations the oscillation is clear in the GONG H α data, but it is not possible to see the filament in absorption in the *SDO* EUV images because of foreground emission. In addition, the structures seen by *SDO* are complex and very dynamic, making the detection of periodic movements very difficult. Therefore we use GONG data to perform our survey of filament oscillations. The GONG network telescopes offer sufficiently good spatial resolution and temporal cadence to detect prominence oscillations with periods of a few 10s of minutes.

The GONG H α images allow us to identify filaments easily and to follow their motions. We interpreted the filament motions as displacements of the prominence plasma in the plane of the sky. However, H α intensity depends on LOS velocities. It is worth mentioning that there exists a possibility that this effect may produce a disappearance of parts of the filament, giving the impression that the remaining visible filament is moving. With the H α GONG data we can study the massive set of oscillations observed since 2010 August, the date when the network started to operate. Here we focus on an analysis of GONG data from several months close to the maximum of solar cycle 24, from 2014 January 1 to June 30. Cycle 24 started in 2008 and reached minimum in early 2010, with a double-peaked maximum in 2013 and 2014.

The GONG network telescopes are of identical design and construction and are placed around the world at the following locations: Learmonth (L), Udaipur (U), El Teide (T), Cerro Tololo (C), Big Bear (B), and Mauna Loa (M). The telescope locations were selected to follow the diurnal motion of the Sun in the sky, in order to collectively ensure full-day coverage (Harvey et al. 1996). Each telescope takes data daily, weather permitting, with some temporal overlap of coverage between telescopes. The temporal cadence of the GONG data is 1 minute, with a pixel size of ~ 1 arcsec. For each data sequence of each telescope we compensate the solar differential rotation using the *drot_map.pro solarsoft* routine. The reference time to de-rotate the images is the central time of each temporal data sequence for each telescope and day.

3. GONG Catalog of Prominence Oscillations

The objective of our GONG catalog is to completely describe the oscillations detected in solar filaments between 2014 January 1 and June 30. The catalog contains information about the properties of the oscillating filaments, the apparent triggers of the oscillation, and the oscillation parameters. With this information, we construct a comprehensive global picture of the filament oscillations close to the maximum of solar cycle 24.

In the following sections we describe the methods we used to construct the catalog (Sections 4–8). The full results of the survey are shown in Tables 1–8. The first group (Tables 1–4) displays data describing the observations and the filaments. The first column corresponds to the number of the oscillation event, ordered in time starting 2014 January 1. The second column lists the telescope where the event is detected (L, U, T, C, B, M). The third column lists the central time of the temporal sequence associated with each telescope used to analyze the event (see Section 2). The fourth column shows the averaged position of the filaments at the reference time (see the detailed description in Section 9). The fifth column indicates the filament type (AR, IT, QS) described in Section 5. The sixth and seventh columns contain the length, L , and width, W , of the filament measured as described in Section 6. In the eighth column we indicate the possible triggering agent described in Section 6. The last column shows whether the filament erupted in the temporal sequence analyzed, indicated by a Y (Yes).

The second group, Tables 5–8, shows the oscillation parameters resulting from the fitting method described in detail in Section 8 with Equation (2). The columns indicate (1) the event number; (2) the initial time of the sequence used for the fit; (3) the angle α between the oscillation direction and the filament spine; (4) the period (P); (5) damping time (τ); (6) damping time per period (τ/P); (7) maximum displacement (A); and (8) velocity amplitude (V).

In Sections 5–8 we will use Event 1 from Table 5 as our reference event to describe the methodology. Although the figures are specific to this event, the results and explanations are valid for all events listed in the tables.

4. Event Selection

Our first action was to detect the filaments that may oscillate by visual inspection of the GONG H α data (<http://gong2.nso.edu>), in which the filaments are seen as dark absorption structures (see Figure 1). The oscillations were identified as periodic displacements of a part of the filament. The GONG webpage shows very good quality movies with full cadence for all six network telescopes. We analyzed daily observations from each telescope, and selected data that showed a clear or suspected oscillatory event for in-depth analysis. In this initial inspection, we identified 408 potential cases. We initially identified each event to be associated with one day and one telescope. For cases where the oscillation continued at the end of the observing period of the selected telescope, we did not utilize the subsequent telescope observations in order to extend the oscillation data. In addition, we checked the data carefully to avoid double counting the same oscillation observed by two telescopes with overlapping data. For cases in which a second oscillation appeared during a given observing period, we

Table 1
Table of the Observation Details and Parameters of the Filament for Events 1–60

Event #	Time	Telescope	Position (x, y)	Type	Length L (Mm)	Width W (Mm)	Trigger	Erupts
1	2014 Jan 1 16:50	C	−18, −76	IP	269	15	FLARE	...
2*	2014 Jan 1 16:50	C	−18, −76	IP	269	15	FLARE	...
3	2014 Jan 4 22:04	B	−251, 302	IP	172	7	FLARE	...
4	2014 Jan 5 17:03	C	−399, 48	IP	87	14	FLARE	...
5	2014 Jan 5 17:03	C	−308, −116	AR	240	13
6*	2014 Jan 5 17:03	C	−308, −116	AR	240	13
7	2014 Jan 5 17:03	C	730, −430	QS	139	10	PE	...
8*	2014 Jan 5 17:03	C	730, −430	QS	139	10	PE	...
9	2014 Jan 5 22:11	B	806, −79	IP	206	11
10	2014 Jan 6 08:59	U	84, 492	QS	44	9	FLARE	...
11	2014 Jan 6 07:11	U	−132, −261	IP	185	8
12	2014 Jan 6 16:56	C	−268, −466	QS	102	8
13	2014 Jan 6 16:56	C	−184, 57	AR	78	12
14*	2014 Jan 6 16:56	C	−184, 57	AR	78	12
15	2014 Jan 6 08:59	U	57, 304	IP	119	8	FLARE	...
16	2014 Jan 7 09:13	U	−335, 78	IP	387	13	FLARE	...
17	2014 Jan 7 09:13	U	−325, −282	IP	190	7	FLARE	...
18	2014 Jan 7 09:13	U	143, −370	IP	445	8
19	2014 Jan 7 16:58	C	−100, −501	QS	143	12	PE	...
20	2014 Jan 8 08:59	U	−139, −316	IP	313	14	PE	...
21	2014 Jan 8 08:59	U	8, −494	IP	187	10
22*	2014 Jan 8 08:59	U	8, −494	IP	187	10
23	2014 Jan 8 08:59	U	260, −367	IP	543	9	FLARE	...
24	2014 Jan 9 17:10	C	155, −306	IP	287	20	FLARE	...
25	2014 Jan 9 17:10	C	242, −505	IP	303	12
26	2014 Jan 10 14:03	T	433, 80	IP	54	9
27	2014 Jan 11 16:43	C	815, −393	IP	221	9	PE	...
28	2014 Jan 15 20:00	B	502, −217	AR	125	6
29	2014 Jan 16 07:37	U	268, 125	AR	80	15
30	2014 Jan 16 19:59	B	−624, −298	IP	228	9
31	2014 Jan 24 17:00	C	−311, −385	IP	281	10	FLARE	...
32	2014 Jan 24 19:11	M	284, −151	IP	394	14
33	2014 Jan 25 07:40	U	−184, −376	IP	251	8
34	2014 Jan 25 16:41	C	−110, −129	AR	163	10	FLARE	...
35*	2014 Jan 25 16:41	C	−110, −129	AR	163	10	FLARE	...
36	2014 Jan 25 16:41	C	508, −95	IP	527	15	FLARE	...
37	2014 Jan 26 08:27	U	850, 99	IP	81	8
38	2014 Jan 27 16:41	C	335, −142	AR	255	9
39*	2014 Jan 27 16:41	C	335, −142	AR	255	9
40	2014 Jan 27 16:41	C	449, −402	IP	209	17
41	2014 Jan 28 20:23	B	635, −420	IP	247	9
42	2014 Jan 29 07:23	U	445, −304	IP	82	11
43	2014 Jan 29 16:49	C	556, −428	IP	251	9
44	2014 Jan 29 19:59	B	−822, 11	IP	182	11	FLARE	...
45	2014 Jan 30 07:23	U	702, 33	IP	195	9	PE	...
46	2014 Jan 31 15:20	C	−557, 16	IP	201	15
47	2014 Feb 1 07:17	U	−404, 58	AR	317	9	FLARE	...
48	2014 Feb 5 17:07	C	−812, −129	IP	206	10	FLARE	Y
49	2014 Feb 5 17:07	C	−212, −269	IP	205	10	FLARE	...
50	2014 Feb 6 17:05	C	−626, −433	IP	363	13	FLARE	...
51	2014 Feb 6 17:05	C	−388, −266	IP	231	10	FLARE	...
52	2014 Feb 7 13:24	T	−506, 243	IP	111	6
53	2014 Feb 8 20:10	B	428, −271	AR	211	9	FLARE	...
54	2014 Feb 8 13:24	T	−193, 114	IP	84	16
55	2014 Feb 8 13:24	T	−122, −162	AR	181	8
56	2014 Feb 9 16:52	C	−82, −93	IP	162	11	FLARE	...
57	2014 Feb 9 16:52	C	−192, −119	IP	109	8	FLARE	...
58	2014 Feb 9 16:52	C	−390, −197	AR	232	7	FLARE	...
59	2014 Feb 11 17:39	C	517, −203	AR	101	9	FLARE	...
60	2014 Feb 12 13:28	T	368, 297	AR	184	8	FLARE	...

Note. In the first column, the asterisk indicates that the oscillation is in the same time–distance diagram than in the previous case.

Table 2
Same as Table 1 for Events 61–120

Event #	Time	Telescope	Position (x, y)	Type	Length L (Mm)	Width W (Mm)	Trigger	Erupts
61	2014 Feb 12 19:42	B	571, -105	IP	160	14	FLARE	...
62	2014 Feb 13 17:05	C	601, 238	AR	236	6	FLARE	...
63	2014 Feb 13 20:04	B	708, -382	QS	721	33	FLARE	...
64	2014 Feb 14 13:27	T	723, 248	AR	295	9	FLARE	...
65	2014 Feb 14 19:34	B	-592, -233	IP	805	8	FLARE	...
66	2014 Feb 16 19:51	B	-17, -93	AR	132	7	FLARE	...
67	2014 Feb 17 07:28	U	-110, -202	IP	898	14	FLARE	...
68	2014 Feb 17 18:52	B	3, -199	IP	1051	13
69	2014 Feb 19 19:47	B	380, -215	IP	913	13	FLARE	...
70	2014 Feb 22 07:28	U	-16, -378	IP	359	9
71	2014 Feb 23 16:55	C	-448, 277	AR	120	12	FLARE	...
72	2014 Feb 24 16:59	C	44, -311	IP	219	22
73	2014 Feb 24 16:59	C	330, -267	IP	200	10
74	2014 Feb 25 16:38	C	548, -213	IP	447	7
75	2014 Feb 25 16:38	C	366, -172	AR	114	8
76	2014 Feb 25 16:38	C	526, 144	QS	46	12	...	Y
77	2014 Feb 27 13:22	T	-1, 164	IP	209	9	FLARE	...
78	2014 Feb 27 16:57	C	-203, 350	IP	147	9
79*	2014 Feb 27 16:57	C	-203, 350	IP	147	9
80	2014 Feb 28 13:22	T	125, -328	QS	813	24
81	2014 Mar 7 17:16	C	590, -74	IP	437	12	FLARE	...
82	2014 Mar 12 07:29	U	-567, -237	IP	210	9	FLARE	...
83	2014 Mar 14 16:58	C	-812, 265	AR	192	8	FLARE	...
84	2014 Mar 16 07:22	U	-539, -213	IP	831	13	PE	...
85	2014 Mar 20 16:59	C	-315, -4	IP	242	9
86	2014 Mar 21 19:21	B	521, 347	AR	335	11	PE	...
87	2014 Mar 23 16:54	C	398, 0	IP	320	12	JET	...
88	2014 Mar 24 18:57	B	586, -13	IP	152	9
89*	2014 Mar 24 18:57	B	586, -13	IP	152	9
90	2014 Mar 28 18:09	B	683, 41	IP	79	18
91	2014 Mar 29 16:57	C	329, 372	IP	120	9	MW	...
92	2014 Mar 29 16:57	C	99, -201	AR	217	6	FLARE	...
93	2014 Mar 30 07:10	U	83, -405	IP	95	10
94	2014 Mar 31 18:49	B	379, -390	IP	289	14	FLARE	...
95*	2014 Mar 31 18:49	B	379, -390	IP	289	14	FLARE	...
96	2014 Apr 7 18:33	B	522, 416	AR	72	6	FLARE	...
97	2014 Apr 9 12:42	T	469, 216	IP	139	9	FLARE	...
98	2014 Apr 9 18:30	M	520, 200	AR	111	8	...	Y
99	2014 Apr 10 05:07	L	653, -431	QS	458	18
100	2014 Apr 14 16:44	C	146, -110	IP	248	10	...	Y
101	2014 Apr 17 05:01	L	-648, -161	IP	531	9	FLARE	...
102	2014 Apr 17 05:01	L	297, 447	QS	210	20
103	2014 Apr 17 16:52	C	5, -324	IP	177	8	PE	...
104	2014 Apr 17 16:52	C	731, -150	QS	141	21
105	2014 Apr 19 04:48	L	602, 466	QS	240	17
106	2014 Apr 19 16:47	C	-185, -125	IP	691	11	FLARE	...
107	2014 Apr 21 18:20	B	701, -371	IP	149	7	FLARE	Y
108*	2014 Apr 21 18:20	B	701, -371	IP	149	7	FLARE	Y
109	2014 Apr 22 16:41	C	61, 296	IP	229	6
110	2014 Apr 23 16:49	C	264, 294	IP	270	7	FLARE	...
111	2014 Apr 24 07:05	U	-262, -263	AR	197	9
112	2014 Apr 24 07:05	U	205, 148	IP	289	11
113	2014 Apr 25 07:10	U	424, 132	IP	264	14
114	2014 Apr 26 13:27	T	465, -370	IP	800	14	PE	...
115	2014 May 1 18:11	B	-380, 231	IP	290	8	FLARE	...
116	2014 May 1 18:11	B	753, -385	IP	428	11	FLARE	...
117	2014 May 1 07:10	U	-625, -379	IP	137	12
118	2014 May 2 07:04	U	-296, 190	AR	212	9	FLARE	...
119*	2014 May 2 07:04	U	-296, 190	AR	212	9	FLARE	...
120	2014 May 2 13:42	T	36, -342	IP	173	12

defined a new event with the same location and telescope as the preceding event, and we marked it with an asterisk next to the event number.

Once we identified the filaments that might oscillate, we downloaded the reduced $H\alpha$ data in the form of FITS files from the GONG server. We de-rotated the images in order to

Table 3
Same as Table 1 for Events 121–180

Event #	Time	Telescope	Position (x, y)	Type	Length L (Mm)	Width W (Mm)	Trigger	Erupts
121	2014 May 5 17:22	B	92, -391	IP	291	8
122	2014 May 10 06:31	U	-499, 417	IP	254	14
123	2014 May 10 13:07	T	-181, -581	QS	71	19	PE	...
124	2014 May 11 18:06	B	-610, -486	QS	395	13	FLARE	...
125	2014 May 12 04:11	L	-142, 443	QS	117	15
126	2014 May 12 04:11	L	77, -22	IP	192	12	FLARE	...
127	2014 May 12 04:11	L	-494, -634	QS	330	10
128	2014 May 12 07:21	U	281, -102	IP	96	9
129	2014 May 12 18:01	M	-346, 361	IP	164	14
130	2014 May 13 18:07	B	323, -26	IP	115	9
131	2014 May 13 18:07	B	-86, -464	IP	222	18
132	2014 May 14 07:22	U	413, -626	QS	149	35
133	2014 May 15 16:43	C	285, 142	IP	330	25
134	2014 May 16 06:47	U	354, 197	QS	246	33
135	2014 May 16 13:07	T	-514, 355	IP	142	9	FLARE	...
136	2014 May 17 04:54	L	521, -70	IP	202	12
137	2014 May 17 13:07	T	649, 135	QS	175	14
138	2014 May 18 19:54	B	455, -96	IP	133	13
139	2014 May 23 12:58	T	-101, 240	IP	228	11
140	2014 May 23 13:07	T	269, -302	IP	292	9
141	2014 May 23 19:27	B	658, 146	QS	164	18
142	2014 May 23 18:10	B	-577, -192	IP	329	9	FLARE	...
143	2014 May 26 03:39	L	243, -432	IP	603	11	FLARE	...
144	2014 May 26 17:08	C	743, -32	QS	97	18
145	2014 May 26 16:45	C	-348, -260	IP	143	10	FLARE	...
146*	2014 May 26 16:45	C	-348, -260	IP	143	10	FLARE	...
147	2014 May 27 04:26	L	280, -233	AR	121	8
148	2014 May 27 11:24	T	552, -404	IP	796	9
149	2014 May 28 04:21	L	-26, -352	AR	219	7	FLARE	...
150	2014 May 29 04:37	L	184, -346	AR	183	8
151	2014 May 30 05:31	L	371, -353	AR	235	11	FLARE	...
152*	2014 May 30 05:31	L	371, -353	AR	235	11	FLARE	...
153	2014 May 30 11:42	T	765, -153	IP	152	8	FLARE	...
154*	2014 May 30 11:42	T	765, -153	IP	152	8	FLARE	...
155	2014 Jun 1 04:36	L	692, -354	AR	123	7	FLARE	Y
156	2014 Jun 2 13:25	T	291, 166	IP	239	19
157	2014 Jun 2 17:45	B	-203, 59	QS	124	19
158	2014 Jun 3 04:32	L	-85, 54	QS	166	15
159	2014 Jun 4 17:42	B	-628, -55	IP	339	10
160	2014 Jun 5 13:09	T	97, -236	IP	256	9
161	2014 Jun 5 19:42	M	-174, 404	QS	98	12
162	2014 Jun 6 13:14	T	323, -235	IP	104	12	...	Y
163	2014 Jun 7 04:45	L	23, -204	IP	108	15
164	2014 Jun 7 13:09	T	-592, -239	IP	206	9
165*	2014 Jun 7 13:09	T	-592, -239	IP	206	9
166	2014 Jun 8 13:09	T	3, 205	AR	290	11
167	2014 Jun 8 17:56	B	-345, -224	IP	355	13
168	2014 Jun 9 13:11	T	242, 212	AR	229	11
169*	2014 Jun 9 13:11	T	242, 212	AR	229	11
170	2014 Jun 9 13:11	T	379, 6	IP	326	17
171	2014 Jun 9 13:11	T	45, -304	AR	166	13
172*	2014 Jun 9 13:11	T	45, -304	AR	166	13
173	2014 Jun 10 18:52	M	499, 220	AR	73	17	FLARE	Y
174	2014 Jun 12 04:33	L	-328, -575	QS	99	12
175*	2014 Jun 12 04:33	L	-328, -575	QS	99	12
176	2014 Jun 12 04:46	U	289, -344	IP	176	13
177*	2014 Jun 12 04:46	U	289, -344	IP	176	13
178	2014 Jun 12 04:33	L	438, -202	IP	166	11
179	2014 Jun 12 12:51	T	469, 490	QS	196	13
180*	2014 Jun 12 12:51	T	469, 490	QS	196	13

compensate for solar rotation and to study the proper motion of the filaments over the solar surface. All images were de-rotated using a reference time that corresponds to the central time of

the temporal sequence, as described in Section 2. This de-rotation algorithm only works on the solar disk, so we discarded events in prominences seen at the limb and focused

Table 4
Same as Table 1 for Events 181–196

Event #	Time	Telescope	Position (x, y)	Type	Length L (Mm)	Width W (Mm)	Trigger	Erupts
181	2014 Jun 13 04:30	L	−163, −574	QS	125	16
182	2014 Jun 13 13:11	T	599, −297	IP	606	19
183	2014 Jun 14 04:40	L	672, −294	IP	288	13
184	2014 Jun 14 13:10	T	745, 55	IP	23	7
185	2014 Jun 14 13:10	T	−527, 490	QS	58	10	FLARE	...
186	2014 Jun 15 17:51	M	−345, 512	IP	86	16	FLARE	...
187*	2014 Jun 15 17:51	M	−345, 512	IP	86	16	FLARE	...
188	2014 Jun 16 13:11	T	−836, 5	IP	189	15
189	2014 Jun 16 13:11	T	−214, 521	IP	61	14
190*	2014 Jun 16 13:11	T	−214, 521	IP	61	14
191	2014 Jun 17 17:56	B	−334, −510	QS	116	12
192	2014 Jun 17 13:12	T	−757, −7	IP	301	13	FLARE	...
193	2014 Jun 17 13:12	T	−39, 520	IP	119	12
194	2014 Jun 17 13:12	T	695, 385	IP	107	7	FLARE	...
195	2014 Jun 19 18:44	M	241, −231	IP	131	13
196	2014 Jun 29 16:50	C	130, −200	IP	691	21

exclusively on filaments seen in absorption on the disk. The coordinates are given in the usual Heliocentric-Cartesian coordinates (Thompson 2006).

5. Filament Classification

In the catalog we assigned filament types exclusively based on GONG $H\alpha$ data, according to the position scheme of Engvold (2015), as active region (AR), intermediate (IT), or quiescent (QS). In Figure 1 we have marked the three types by colored arrows (AR—red, IT—green, QS—blue). AR filaments are located close to sunspots and plages with a prominent spine and few or no barbs. ITs have one end close to an AR and the other end far from an AR; they exhibit both a spine and barbs. The QSEs are far from any AR or plage region, with no clear spine. For filaments whose type was difficult to determine, we used *SDO* HMI magnetograms to distinguish whether the filament is close to a strong magnetic field or a quiet region. The catalog includes 45 AR, 99 IT, and 52 QS filaments.

Following this classification, we identify our reference case 1 as *intermediate*, or IT (see Table 1), because the filament has one end located in the plage associated with the AR NOAA 11938 and the other end in a quiet region (see Figure 2).

6. Triggering and Filament Parameters

We constructed a movie with the FITS data showing the region of interest surrounding each filament, enabling us to identify the most likely triggering agent and to study the filament motion. For more than half of the events, we could not identify what triggered the oscillations, so we left column 4 empty in Tables 1–4. Those cases for which we found a trigger were marked FLARE when a sudden $H\alpha$ brightening was detected nearby just before the oscillation onset, prominence eruption (PE) when a nearby filament erupted before oscillation onset, and JET when the trigger was a jet of plasma that hit the filament. In one case, 91, we clearly observed a Moreton wave (MW) emanating from a flare and hitting the filament, triggering its oscillation as described in Section 9.3.

In Figure 2 the sequence of events is shown for our reference case 1. The trigger was identified as a flaring region located south of the filament. In order to parametrize the flare position, we averaged the measured positions of several bright regions in

the flare; this averaged position is marked by a red dot in Figure 2(a). This panel also shows the equilibrium position of the filament before the trigger perturbed the filament. Panels (b) and (c) show the difference images at the given times with the image shown in (a) subtracted, thus visualizing the displacements with respect to the equilibrium configuration. The initial motion was in the northwest direction (Figure 2(b)), and then the motion was reversed to travel toward the southeast (Figure 2(c)).

Because the filaments were very dynamic and their shapes changed considerably during the observation intervals, we first generated an average image of the region of interest, as shown in Figure 3 for case 1. This image was constructed by averaging 10 equally spaced images from the data sequence of the day and telescope selected (i.e., Cerro Tololo or C in this case). From this averaged image we determined the position of the spine following the dark filament (thick white line in Figure 3); the length of the spine, L ; and the average width of the filament, W . We defined the width of the filament at five equidistant positions along the spine as the length of the five segments plotted in the figure as thin lines. The average width and length characterize the size of the filament, to be used later in our statistical study. For this example, the length is $L = 269$ Mm and width $W = 15$ Mm (see event 1 in Table 1). Using the positions of the filament spine, we also obtained the averaged position of the filament on the solar disk, marked with a cross in the figure.

7. Time–Distance Diagrams and Direction of the Motion

We used the time–distance approach to analyze the filament oscillations. Because many oscillations reported in this work did not follow straight trajectories, but rather moved along curved paths, we could not apply the technique described by Luna et al. (2014) based on straight slits. In addition, due to the relatively low resolution of the GONG data, we needed to generate time–distance diagrams with minimal reduction of the effective resolution in curved slits. To define the curved slit in the $H\alpha$ images for each event, we tracked the path of the oscillations by visual inspection. In order to generate the slit, we first traced the motion of the filament segment with the clearest and largest displacement. The slit, of length l and width w pixels, was placed lengthwise along the curved path of the

Table 5
Table of Oscillation Best-fit Parameters for 1–60

#	Initial Time	$\alpha(^{\circ})$	P (minutes)	τ (minutes)	τ/P	A (Mm)	V (km s $^{-1}$)
1	2014 Jan 1 13:50	16	76 ± 2	121 ± 15	1.6 ± 0.2	22 ± 2	26.5 ± 3.6
2*	2014 Jan 1 18:56	16	71 ± 3	173 ± 107	2.4 ± 2	8 ± 3	10.7 ± 7.0
3	2014 Jan 4 20:30	26	57 ± 2	105 ± 33	1.8 ± 0.6	4 ± 1	8.0 ± 3.5
4	2014 Jan 5 11:43	9	63 ± 4	5 ± 3	9.4 ± 9.2
5	2014 Jan 5 12:01	32	52 ± 1	1 ± 1	2.7 ± 6.0
6*	2014 Jan 5 17:05	32	76 ± 3	−115 ± 38	−1.5 ± 0.6	3 ± 1	3.5 ± 6.0
7	2014 Jan 5 10:44	0	63 ± 3	−390 ± 545	−6.2 ± 9	2 ± 1	3.9 ± 6.7
8*	2014 Jan 5 21:31	0	43 ± 3	160 ± 329	3.7 ± 8	5 ± 3	10.7 ± 11.1
9	2014 Jan 5 20:13	37	44 ± 2	38 ± 9	0.9 ± 0.2	5 ± 2	11.6 ± 6.2
10	2014 Jan 6 06:58	22	68 ± 1	617 ± 367	9.0 ± 5	8 ± 1	12.4 ± 1.9
11	2014 Jan 6 08:02	23	63 ± 2	94 ± 23	1.5 ± 0.4	4 ± 1	5.5 ± 3.8
12	2014 Jan 6 11:07	38	40 ± 3	158 ± 141	4.0 ± 4	2 ± 1	6.5 ± 7.9
13	2014 Jan 6 12:27	16	61 ± 1	118 ± 18	1.9 ± 0.3	10 ± 1	15.4 ± 2.1
14*	2014 Jan 6 16:26	16	56 ± 6	475 ± 1313	8.5 ± 20	3 ± 2	5.6 ± 11.5
15	2014 Jan 6 06:45	1	64 ± 1	8 ± 1	12.8 ± 1.7
16	2014 Jan 7 05:58	14	65 ± 2	302 ± 158	4.7 ± 3	4 ± 1	6.2 ± 3.6
17	2014 Jan 7 04:04	3	46 ± 1	96 ± 24	2.1 ± 0.5	5 ± 1	11.0 ± 4.3
18	2014 Jan 7 04:45	23	50 ± 1	46 ± 5	0.9 ± 0.1	15 ± 2	25.5 ± 4.7
19	2014 Jan 7 14:16	26	44 ± 1	83 ± 8	1.9 ± 0.2	14 ± 2	31.2 ± 4.5
20	2014 Jan 8 05:47	30	50 ± 2	67 ± 15	1.4 ± 0.3	15 ± 3	36.5 ± 8.8
21	2014 Jan 8 04:49	2	43 ± 2	100 ± 45	2.3 ± 1	4 ± 1	9.0 ± 4.7
22*	2014 Jan 8 08:18	2	35 ± 2	1 ± 1	2.5 ± 9.3
23	2014 Jan 8 03:28	24	59 ± 1	102 ± 14	1.7 ± 0.2	7 ± 1	14.7 ± 2.9
24	2014 Jan 9 16:56	40	51 ± 2	97 ± 29	1.9 ± 0.6	5 ± 2	9.3 ± 5.7
25	2014 Jan 9 12:31	44	46 ± 3	73 ± 33	1.6 ± 0.8	4 ± 2	10.8 ± 7.5
26	2014 Jan 10 11:23	45	43 ± 2	80 ± 26	1.9 ± 0.7	3 ± 1	10.2 ± 5.5
27	2014 Jan 11 12:37	24	66 ± 3	114 ± 51	1.7 ± 0.8	2 ± 1	2.7 ± 7.5
28	2014 Jan 15 17:38	35	39 ± 1	78 ± 13	2.0 ± 0.3	7 ± 2	16.2 ± 5.8
29	2014 Jan 16 08:29	13	53 ± 2	232 ± 168	4.4 ± 3	2 ± 1	3.1 ± 5.4
30	2014 Jan 16 20:46	12	57 ± 2	58 ± 10	1.0 ± 0.2	9 ± 2	18.8 ± 6.1
31	2014 Jan 24 17:17	26	77 ± 4	663 ± 1546	8.6 ± 20	1 ± 1	1.6 ± 9.5
32	2014 Jan 24 21:00	21	94 ± 2	17 ± 2	20.4 ± 3.5
33	2014 Jan 25 07:16	34	72 ± 2	94 ± 20	1.3 ± 0.3	4 ± 1	4.4 ± 3.0
34	2014 Jan 25 12:19	37	34 ± 3	103 ± 185	3.0 ± 6	1 ± 1	3.1 ± 12.9
35*	2014 Jan 25 14:47	37	50 ± 2	46 ± 6	0.9 ± 0.1	9 ± 2	25.2 ± 6.5
36	2014 Jan 25 16:06	15	87 ± 1	185 ± 26	2.1 ± 0.3	23 ± 2	28.6 ± 3.1
37	2014 Jan 26 08:09	36	74 ± 1	343 ± 117	4.6 ± 2	5 ± 1	7.8 ± 2.7
38	2014 Jan 27 14:28	27	45 ± 3	−189 ± 216	−4.2 ± 5	2 ± 1	4.5 ± 10.7
39*	2014 Jan 27 20:02	27	55 ± 2	172 ± 112	3.1 ± 2	4 ± 1	7.4 ± 5.2
40	2014 Jan 27 16:04	39	52 ± 1	327 ± 154	6.3 ± 3	2 ± 1	4.4 ± 3.8
41	2014 Jan 28 20:14	29	59 ± 3	101 ± 35	1.7 ± 0.6	6 ± 2	11.0 ± 5.1
42	2014 Jan 29 08:23	7	59 ± 2	131 ± 34	2.2 ± 0.6	4 ± 1	8.2 ± 3.2
43	2014 Jan 29 19:36	35	52 ± 2	424 ± 617	8.2 ± 10	2 ± 1	4.7 ± 8.1
44	2014 Jan 29 18:35	26	69 ± 2	4 ± 1	6.5 ± 4.2
45	2014 Jan 30 05:20	28	62 ± 1	117 ± 14	1.9 ± 0.2	6 ± 1	11.7 ± 2.6
46	2014 Jan 31 13:40	28	44 ± 1	72 ± 10	1.6 ± 0.2	10 ± 2	21.0 ± 3.7
47	2014 Feb 1 07:55	39	59 ± 10	159 ± 264	2.7 ± 5	1 ± 1	2.4 ± 15.4
48	2014 Feb 5 13:53	26	52 ± 2	150 ± 58	2.9 ± 1	4 ± 2	7.7 ± 6.4
49	2014 Feb 5 20:03	44	54 ± 3	2 ± 1	3.7 ± 8.7
50	2014 Feb 6 16:45	30	68 ± 2	78 ± 13	1.2 ± 0.2	11 ± 2	15.6 ± 4.5
51	2014 Feb 6 17:26	34	60 ± 2	105 ± 20	1.8 ± 0.4	9 ± 2	12.2 ± 4.2
52	2014 Feb 7 09:44	30	67 ± 2	140 ± 29	2.1 ± 0.5	8 ± 2	13.0 ± 3.5
53	2014 Feb 8 21:28	64	47 ± 1	61 ± 5	1.3 ± 0.01	13 ± 1	22.9 ± 2.5
54	2014 Feb 8 10:57	68	36 ± 1	194 ± 140	5.3 ± 4	1 ± 1	2.8 ± 5.9
55	2014 Feb 8 10:34	25	36 ± 1	2 ± 1	5.5 ± 7.0
56	2014 Feb 9 14:10	35	63 ± 1	78 ± 8	1.2 ± 0.1	22 ± 3	46.2 ± 5.0
57	2014 Feb 9 15:04	42	37 ± 1	1 ± 1	3.9 ± 7.0
58	2014 Feb 9 11:48	32	47 ± 1	82 ± 20	1.8 ± 0.4	5 ± 2	14.0 ± 5.0
59	2014 Feb 11 17:13	35	57 ± 1	72 ± 6	1.3 ± 0.01	14 ± 2	25.7 ± 3.3
60	2014 Feb 12 14:19	18	55 ± 1	283 ± 170	5.1 ± 3	3 ± 1	6.3 ± 4.7

Note. In first column, the asterisk indicates that the oscillation is in the same time–distance diagram than in previous case.

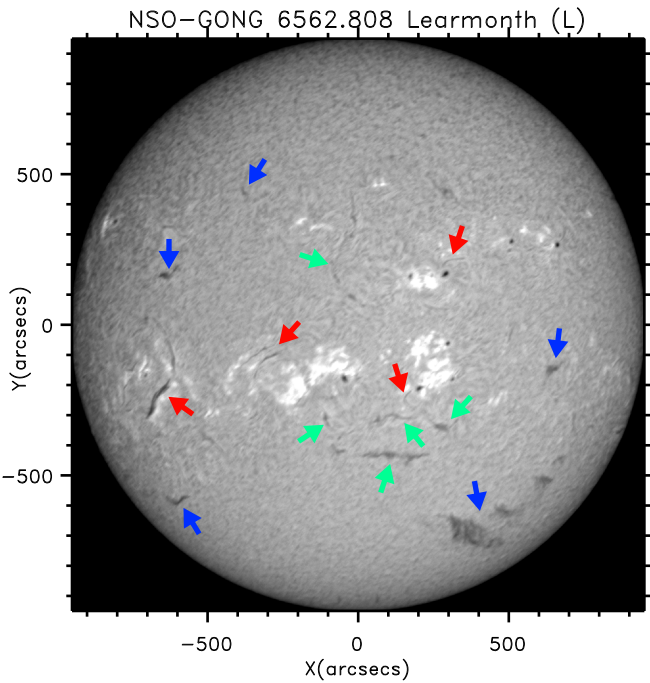


Figure 1. GONG $H\alpha$ image from the Learmonth telescope illustrating the three types of filaments, which are seen as dark structures against the bright chromosphere. The red arrows point to active region (AR) filaments; green arrows point to intermediate filaments (IT) between ARs; blue arrows point to quiescent (QS) filaments.

motion, as described in the [Appendix](#). With the technique shown in the [Appendix](#), we averaged the intensity over the transverse pixels, w , resulting in an intensity distribution along l . The time–distance diagrams display this intensity along the slit as a function of time. Figure 2 shows that the slit matches the trajectory of the cool plasma for case 1. The vertical coordinate in the time–distance diagrams (e.g., Figure 2(a)) corresponds to the distance along the slit in Mm, with the origin set to coincide approximately with the equilibrium position of the filament. This distance is measured in the plane of the sky in x – y coordinates (i.e., Heliocentric-Cartesian coordinates); thus the displacements are projections of the actual motions onto the plane of the sky. Similarly, the velocities measured in the time–distance diagrams are also projections, so the actual values are probably larger.

The angle α between the direction of the oscillatory motion and the filament spine was measured at the intersection of the spine curve and the slit (orange curve in Figure 3). This angle (dotted arc) characterizes the polarization of the oscillations in terms of longitudinal or transverse movements. In this example, $\alpha = 16^\circ$ (see Table 5), so the oscillation is longitudinal. In case 1, we found that the triggering location was aligned with the slit used to track the motion (Figure 3), suggesting that the perturbation from the flare followed the same direction as the slit to reach the filament. The angle α is a projection onto the sky plane of the actual angle. The difference between these angles depends on the filament’s position and orientation on the solar disk.

Using the technique explained in the [Appendix](#), we constructed time–distance diagrams for each event. In the resulting time–distance diagram for our reference case 1 (Figure 4(a)), the filament appears as a dark band surrounded by bright emission from the adjacent chromospheric plasma, and the filament oscillations are clearly visible.

The slit was traced visually following the motion of the cool plasma in the $H\alpha$ images, introducing a subjective factor in the determination of the slit path. In addition, the relatively low spatial resolution of GONG data could produce a misalignment of the slit with the actual trajectory of the cool plasma, reducing the measured displacements over the slit and yielding another source of error in the measurements of the displacements. We have not quantified explicitly the error introduced by the misalignment, however, because we have overestimated the errors in the displacements as discussed in Section 8.1. Additionally, the misalignment introduces an error in α , but it is unclear how to assess the uncertainties in this parameter. We are currently developing automated techniques to track the motion of the filament, which will enable us to quantify and reduce the errors in the displacement and α .

8. Oscillation Analysis

To determine the central position of each filament as a function of time, we plotted the intensity along the slit and fitted a Gaussian function to the intensity for each image of the observing sequence. Because the absorption of the filament depends on the column depth of cool plasma along the LOS, we assumed that the intensity minimum corresponds to the central position in the direction along the slit. This Gaussian function also enabled us to determine the uncertainties of the oscillatory parameters (Section 8.1). We used the *gaussfit.pro* IDL routine with a functional form

$$I(s) = g_0 e^{-\frac{1}{2}\left(\frac{s-s_0}{g_1}\right)^2} + g_2 + g_3 s + g_4 s^2, \quad (1)$$

where s is the coordinate along the slit, $g_0 < 0$ is the intensity amplitude, s_0 is the central position of the Gaussian, $g_1 = \sigma_G$ is the standard deviation, and the remaining terms are the background chromospheric emission.

Figure 5 shows the intensity along the slit at $\sim 16:06$ UT (blue vertical line in Figure 4(a)) in the reference case, with the position of the local minimum indicated by an asterisk. To avoid errors due to noisy data, we consistently used the central position of the Gaussian function, $s_0(t)$, to track the filament motion (see Figure 4(b) for case 1). The measured velocity for all events was derived from the observations by computing the numerical derivative of $s_0(t)$. The function used to fit the oscillation is an exponentially decaying sinusoid, plus a third-order polynomial function to de-trend the proper motions of the filament:

$$y(t) = A_0 e^{-A_1(t-t_0)} \cos [A_2(t-t_0) + A_3] + A_4 + A_5(t-t_0) + A_6(t-t_0)^2 + A_7(t-t_0)^3, \quad (2)$$

where A_i are the coefficients of the fit. Sometimes the beginning of the oscillation is not well described by Equation (2), so we performed the fit in a selected time interval when the oscillation is clear in the time–distance diagram for each event. In Equation (2), t_0 is the initial time of the fitted function (column 2, Tables 5–8). The first few coefficients of the fit are associated with the oscillation in the following way: A_0 is the fitted displacement amplitude; $A_1 = 1/\tau$, where τ is the damping time; $A_2 = 2\pi/P$, where P is the period; and A_3 is the initial phase. The remaining terms are the coefficients of the polynomial function that fits the background motion of the filament. This trend function filters

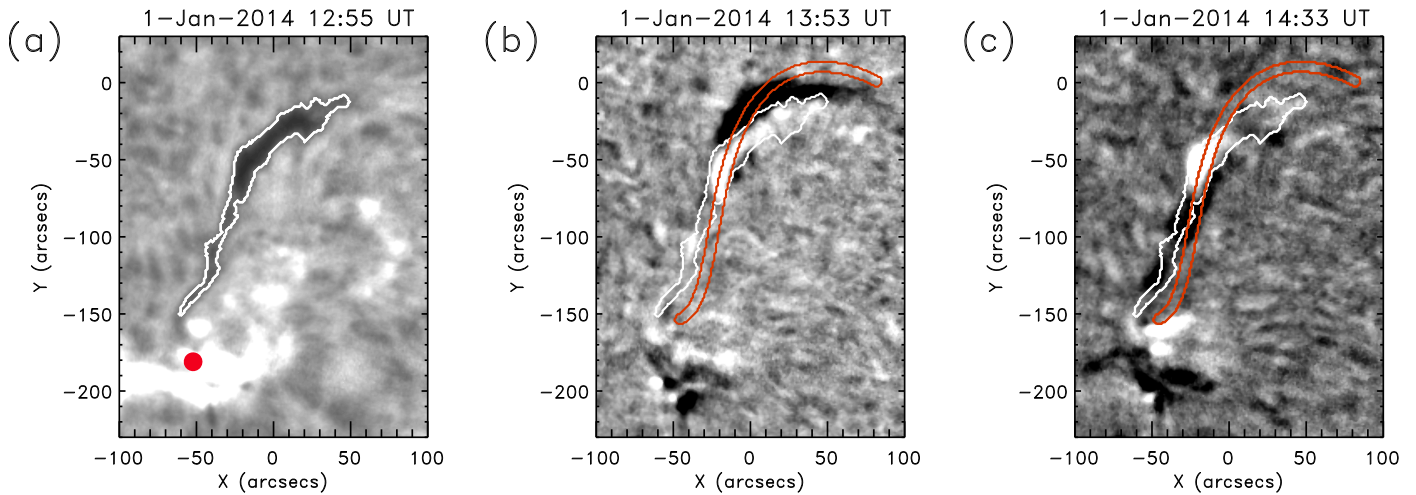


Figure 2. Temporal sequence of the triggering and oscillations in event 1. (a) $H\alpha$ image showing the dark filament in its equilibrium position (12:55 UT, before oscillation onset), outlined by a white contour. The brightening associated with the triggering flare and the averaged flare position (red dot) are also visible. (b) Base difference $H\alpha$ image (13:53 UT–12:55 UT) showing the northward displacement of the filament. The dark and white regions correspond to negative and positive differences, respectively. The contour of the equilibrium filament is overplotted in white. (c) Base difference $H\alpha$ image (14:33 UT–12:55 UT) showing the southern displacement of the central part of the filament. In (b) and (c) the orange contour marks the slit used to track the filament motion.

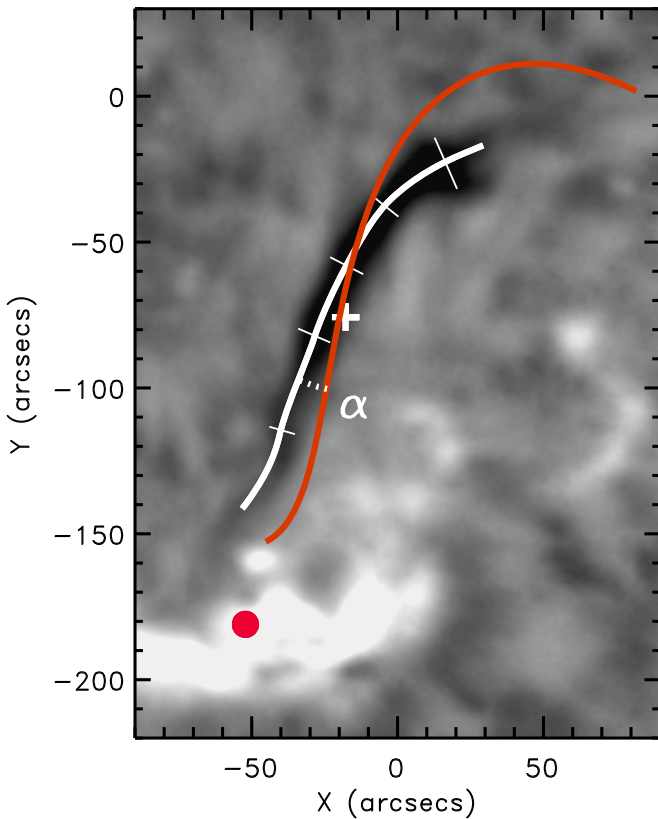


Figure 3. $H\alpha$ image of event 1 averaged over 10 equally spaced times from the full observing period, showing the spine position (white line), the spine length (L), and the average filament width (W). The 5 thin line segments were used to calculate the average width of the dark band. The orange contour corresponds to the slit used to follow the motion and to construct the time–distance diagrams. α measures the angle between the direction of motion (i.e., the slit) and the filament spine. In this example, $\alpha = 16^\circ$, $L = 260$ Mm, and $W = 15$ Mm. The red dot marks the averaged flare position; the white cross is the averaged filament position on the solar disk.

out motions associated with long-period oscillations. Very long periods have been observed in a few oscillating filaments (Foullon et al. 2004, 2009; Efremov et al. 2016), but these

motions are not clear in our data. Hence we focus our attention on more rapid oscillations.

Figure 4(c) shows the measured velocity (diamonds) and the best fit obtained from Equation (2) (solid curve) for case 1. The filament remained essentially stationary before 13:00 UT; then the velocity increased slowly between 13:00 and 13:30 UT. In the following ≈ 30 minutes, the velocity suddenly jumped up to 60 km s^{-1} , returned to zero at the time of maximum displacement (see Figure 4(b)), and increased again in the opposite direction to -55 km s^{-1} . In this phase the acceleration reached 140 m s^{-2} . The velocity does not resemble a sinusoidal oscillation until after $\sim 14:00$ UT. The measured velocity and the fitted function agree very well.

8.1. Errors

Several sources of uncertainty in the measured oscillation parameters are attributable to the relatively low spatial resolution of the GONG images, including jitter, the uncertainties in the exposure time, and the above mentioned misalignment of the slit with the cool plasma trajectories. We assumed that the uncertainty in the oscillation parameters comes mainly from the errors in determining the position of the filament along the slit. In Figure 6 we have plotted a time–distance diagram in an interval where no oscillation was evident. The asterisks mark the central positions of the Gaussian fit, $s(t)$. We clearly see a noisy signal in the figure, where the 1σ standard deviation (thin straight lines) around the mean value is $\sigma_{\text{noise}} = 1.4$ Mm. The figure also shows the width of the Gaussian fit, σ_G , to the intensity (Equation (1)) as dashed lines, which coincide with the borders of the dark band. We consider σ_G to overestimate the uncertainty of the central position, because this uncertainty is comparable to the filament width. In fact, $\sigma_G \gtrsim 3\sigma_{\text{noise}}$ in all analyzed events. Thus we decided somewhat arbitrarily to set the uncertainty of the filament position as $\sigma = 0.5 \sigma_G \gtrsim \sigma_{\text{noise}}$ (indicated by two solid curves in Figure 6). This overestimates the error because $\sigma > \sigma_{\text{noise}}$ and the uncertainty in the position is larger than the variations seen in the figure. This error σ will be considered the

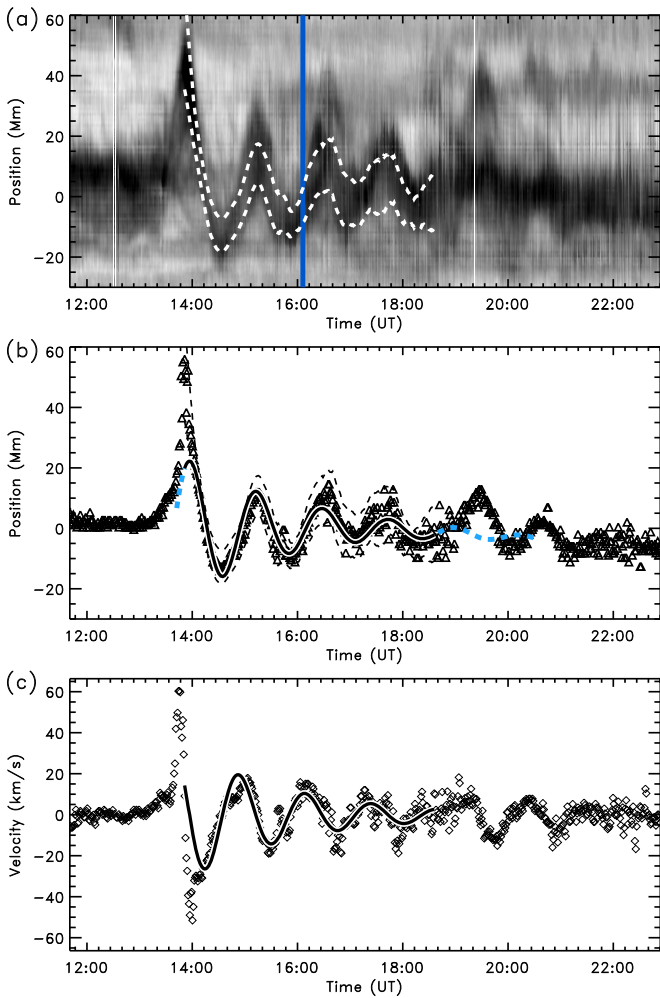


Figure 4. Oscillation diagnostics of event 1. (a) Time–distance $H\alpha$ diagram. The dark band is the filament seen in absorption, surrounded by bright emission from the adjacent chromosphere. The two dashed lines mark the 1σ level as discussed in Section 8.1. (b) Triangles show the central position of the filament, $s_0(t)$, as a function of time t as determined from the Gaussian fit along the slit using Equation (1). The 1σ region is delimited by two thick dashed lines. The thick solid line is the best fit to the triangles using Equation (2). The blue dashed line is the same fitted function extrapolated to times outside the temporal range used to construct the fit. (c) The velocity as a function of time, computed as the time derivative of $s_0(t)$. The velocity obtained with the fitted function (2) is overlotted as a solid curve.

only source of uncertainty in the estimated oscillation parameters.

In Table 5 we have tabulated the best-fit parameters from Equation (2) for all oscillation events. Event 1 has a period of $P = 76 \pm 1$ minutes, damping time $\tau = 121 \pm 15$ minutes, maximum displacement $A = 23 \pm 2$ Mm, and peak velocity amplitude $V = 26 \pm 4$ km s⁻¹. The ratio $\tau/P = 1.6 \pm 0.2$, indicating that the damping was strong and very efficient. Because the velocity amplitude was larger than 10 km s⁻¹, event 1 is a LAO. Large velocities exceeding 40 km s⁻¹ occurred early in this event, but this phase did not produce a fit compatible with subsequent motions (Figure 4(c)). The best fit derived from Equation (2) has a much lower peak value of 26 km s⁻¹ and agrees well with most of the subsequent velocity oscillations. At the end of the fitted range, around 18:30 UT, the first oscillation ceased and a new one appeared. This new oscillation, case 2*, had a different phase and amplitude than case 1, which can be seen by comparing the observed triangles

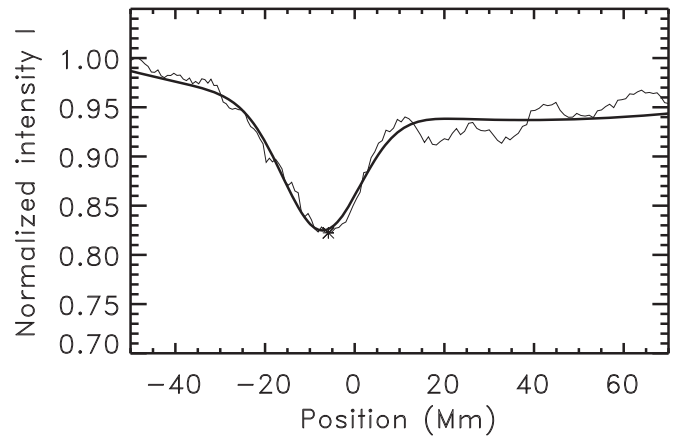


Figure 5. $H\alpha$ intensity along the slit for case 1 at 16:06 UT (thin line), corresponding to the blue vertical line in Figure 4(a). An asterisk marks the intensity minimum. The thick line is the Gaussian fit to the observed intensity profile using Equation (1).

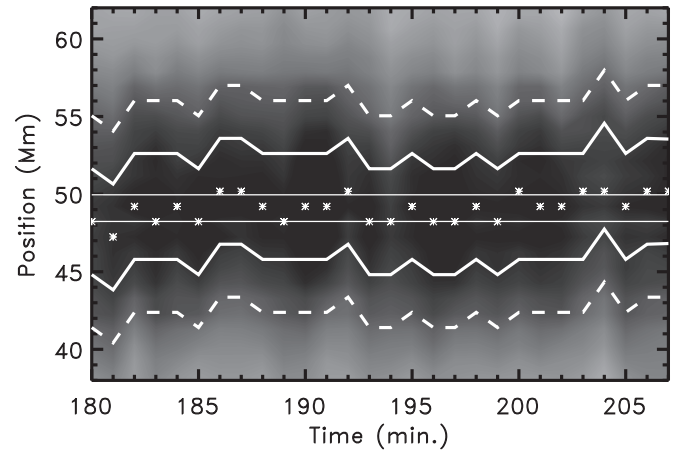


Figure 6. Time–distance diagram of an interval with no clear oscillations. The asterisks mark the central positions of the Gaussian fit of Equation (1), $g_1(t)$. The standard deviation of these points is σ_{noise} ; the two thin horizontal lines correspond to $\pm\sigma_{\text{noise}}$ with respect to the mean value of these positions. The two dashed curves are at $g_1 \pm \sigma_G$, containing the dark region in the diagram. We use $\sigma = 0.5\sigma_G$ as the uncertainty in the filament position. Here the uncertainty region $g_1 \pm \sigma$ is delimited by two solid lines.

with the blue dashed line from the fit of case 1 in Figure 4(b). Cases 1 and 2* have comparable periods, indicating that they are characteristic oscillations of the filament. The direction of the motion is offset by 16° from the filament spine (see Figure 3(b) and Table 5), suggesting that the oscillation is longitudinal as well as large-amplitude (i.e., a LALO). This angle is comparable to the typical angle between the magnetic field and the filament spine, according to direct measurements (Leroy et al. 1983, 1984; Tandberg-Hanssen 1995; Trujillo Bueno et al. 2002; Casini et al. 2003; López Ariste et al. 2006), suggesting that the oscillation is aligned with the filament magnetic field.

9. Selected Case Studies

In the previous sections we used case 1 as a representative oscillation example from our event catalog. Here we describe

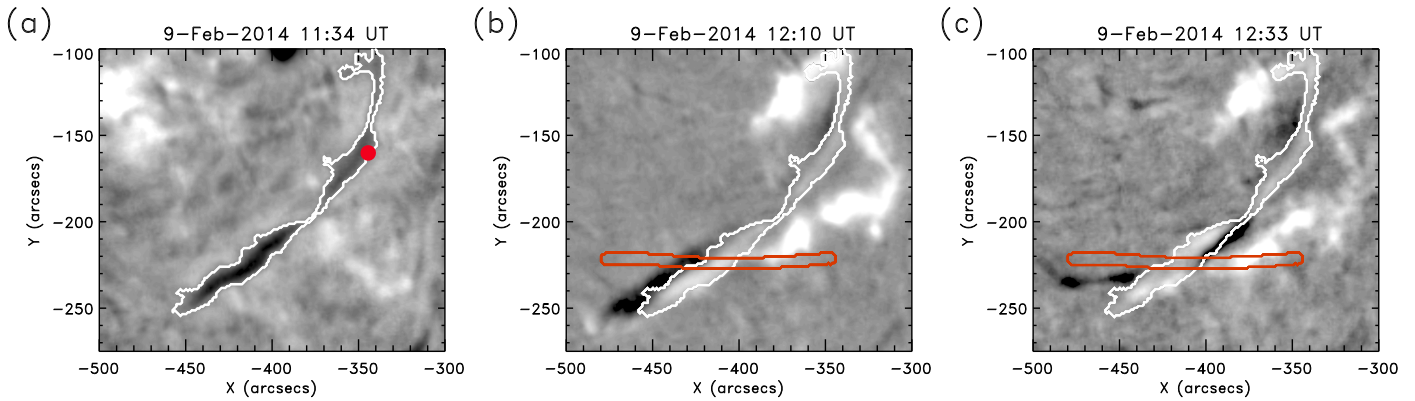


Figure 7. Temporal sequence of the triggering and oscillations in event 58. Panels and annotations are as in Figure 2. (a) Pre-oscillation $H\alpha$ image at 11:34 UT. The white contour outlines the equilibrium filament position at flare onset (11:24 UT). The triggering two-ribbon flare is not visible in this initial frame. The red dot marks the average position of the flaring region (evident in (b)). (b) Base difference $H\alpha$ image (12:10 UT–11:34 UT). The two flare ribbons appear as bright patches north and south of the filament. (c) Base difference $H\alpha$ image (12:33 UT–11:34 UT).

selected additional events from the catalog to illustrate the intriguing variety of behaviors and oscillation characteristics encountered in our survey.

9.1. Event 58: LALO Triggered by a Two-ribbon Flare

Event 58 of the survey (Table 5) is a LAO with a peak velocity of 14 km s^{-1} , triggered by a two-ribbon flare that straddled the AR filament (see Figure 7(a)). This flare produced an oscillation in which the cool plasma was displaced initially in the west–east direction from its pre-flare equilibrium position (white contour in Figure 7(a)). Then the motion was reversed, so the filament reached maximum western elongation (Figure 7(b)), followed by another reversal that produced a peak eastward displacement of smaller amplitude (Figure 7(c)). The figure also demonstrates that the slit used to track the motion and construct the time–distance diagram closely follows the trajectory of the cool filament plasma. Very clear oscillations in the $H\alpha$ intensity are evident in Figure 8(a), triggered around 11:50 UT and lasting for more than seven periods from $\sim 12:00$ to 18:00 UT. Before flare onset the dark filament band is almost horizontal, so the filament was almost at rest. In Figure 8(b), the central position $s(t)$ and its best fit from Equation (2) agree well until $\sim 16:00$ UT. Thereafter the fit is more damped than $s(t)$, and a slight phase difference is also evident. After 19:00 UT the measured $s(t)$ is very noisy because the quality of the $H\alpha$ images was reduced.

The fitted velocity matches the measured velocity well (Figure 8(c)). There were no large velocities during the initial phase associated with the triggering, in contrast with case 1 (Figure 4(c)). Although the initial velocity exceeded 10 km s^{-1} , indicating that this event is a LAO, in less than a period the velocity fell below this threshold. The direction of motion was offset by 32° from the filament spine, identifying this event as a possible LALO.

9.2. Event 63: LALO in a Large Quiescent Filament

In case 63 the oscillation occurred in a very large, fragmented *quiescent* filament (QS) in the southern hemisphere. The oscillation appeared in the southern segment, possibly triggered by the flare centered at the red dot in Figure 9(a). The $H\alpha$ flare brightened slightly before the oscillation began at $\sim 18:26$ UT. Part of the prominence plasma moved toward the northwest or west along a curved trajectory.

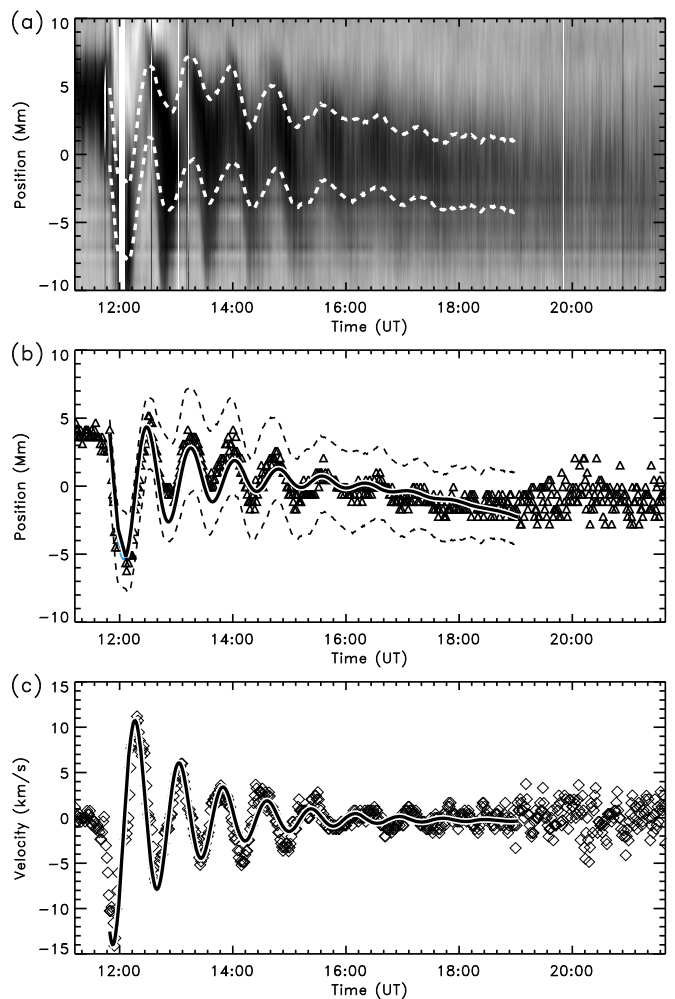


Figure 8. Oscillation diagnostics of event 58. Panels and annotations are as in Figure 4.

Difference images in Figures 9(b) and (c) reveal the maximum elongation at two times after the initiation: a dark region along the slits appeared, first on one side and then on the other side of the pre-oscillation position of the filament (Figure 9(c)).

Several threads of cool plasma moved in a complex way before oscillation onset at 20:26 UT (Figure 10(a)). Thereafter the oscillation was very clear but only was observed for two

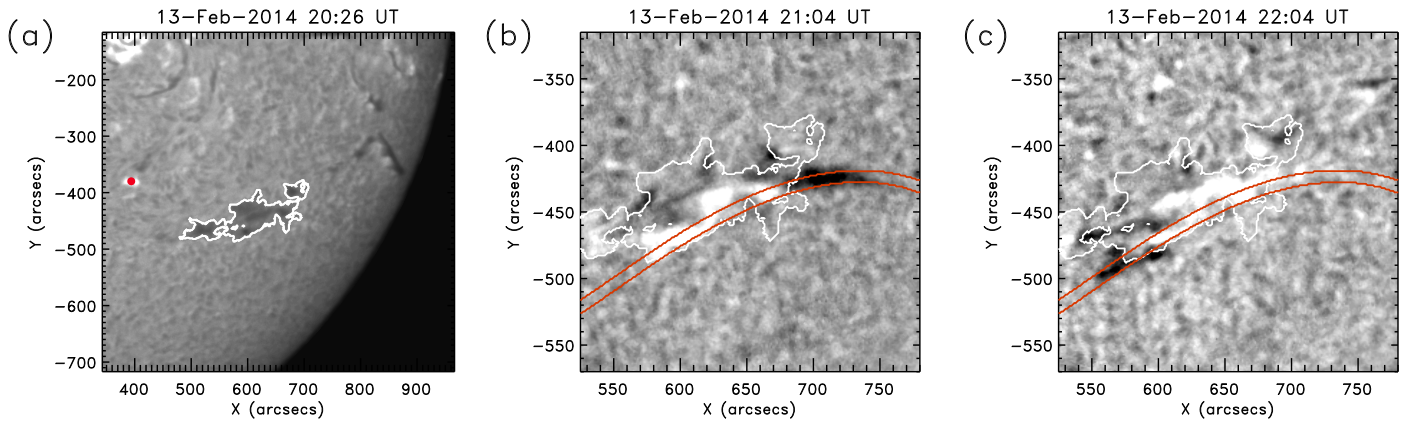


Figure 9. Temporal sequence of the triggering and oscillations in event 63. Panels and annotations are as in Figure 2. Here panels (b) and (c) show a smaller region centered at the filament. (a) Pre-oscillation H α image at 20:26 UT. (b) Base difference H α image (21:04 UT–20:26 UT), showing the initial northwestward displacement of the filament along the slit. (c) Base difference H α image (22:04 UT–20:26 UT), showing the subsequent southeastward displacement.

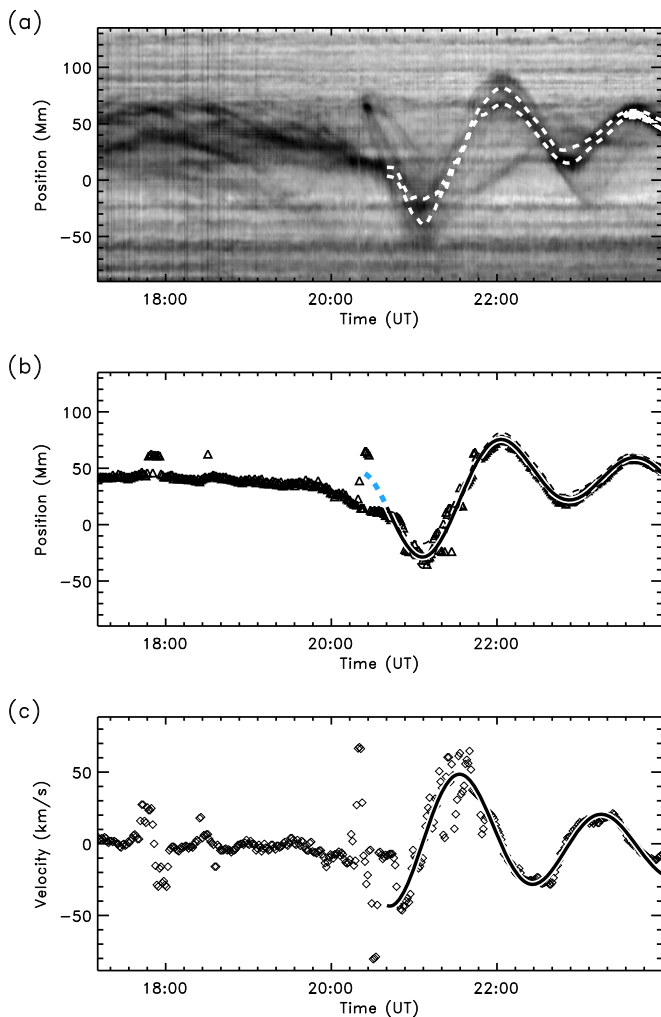


Figure 10. Oscillation diagnostics of event 63. Panels and annotations are as in Figure 4.

cycles. Apparently the whole filament was displaced to the southeast before the oscillation, possibly indicating that the structure of the filament changed during the pre-flare phase. In Figure 10(a) the positional uncertainty, σ , is indicated by two dashed lines. This uncertainty is very small where the dark band is very narrow. Initially some threads moved toward the

centroid of the oscillation, but our tracking code ignored these outliers and only followed the motion of the main body, the darkest band at $s \sim 10$ Mm. After 20:39 UT, the entire filament oscillated, and Equation (2) provided a good fit to $s(t)$ (Figure 10(b)). The measured velocity amplitude, V , reached very large values >50 km s $^{-1}$ (Figure 10(c)).

The results of the fit are shown in Table 5. The oscillation had a velocity amplitude of $V = 48.5 \pm 2.4$ km s $^{-1}$, $P = 103 \pm 1$ minutes, a damping time $\tau = 175 \pm 12$ minutes, and $\tau/P = 1.7 \pm 0.1$, indicating very strong damping. The motion was only $\alpha = 2^\circ$ misaligned with the filament spine, indicating that this event was probably a LALO.

9.3. Event 91: LALO Triggered by a Moreton Wave

Event 91 occurred in an intermediate filament (IT) located close to AR NOAA 12017. Around 17:41 UT, a major flare occurred in the AR followed by an MW, which is visible in Figure 11. This is the only event in the survey for which we could identify an MW connected to the filament oscillation. The wave emanated from the flare region (Figure 11(a)), hit the filament (Figure 11(b)), and then continued to propagate northward (Figure 11(c)). Once the wave encountered the filament (Figure 12(b)), the filament started to oscillate perpendicular to the propagation direction of the wave front. At 18:53 UT (Figure 12(c)), the motion was reversed and the oscillatory motion was fully established. The time–distance diagram in Figure 13(a) reveals significant motions of the filament before and after flare onset. Around oscillation onset, at 17:47 UT, a white vertical region appears in Figure 13(a), signalling the arrival of the MW at the filament throughout the slit. The MW initially produced complex filament dynamics, best seen in a movie of the event (not shown here). The oscillation became distinct around 18:00 UT, with a maximum southeastward displacement of 12 Mm from the equilibrium position around 18:22 UT (Figure 13(b)) and a smaller opposing displacement at 18:53 UT (Figure 13(b)). Interestingly, when the filament moved in the northwest direction, it was darker than when the motion was in the opposite direction (Figure 13(a)). The central position of the dark band oscillated clearly (Figure 13(b)), and was fitted very well with Equation (2) after 18:23 UT. However, between the triggering at 17:47 UT and 18:23 UT, the motion does not fit the sinusoidal function (blue dashed line), probably due to the

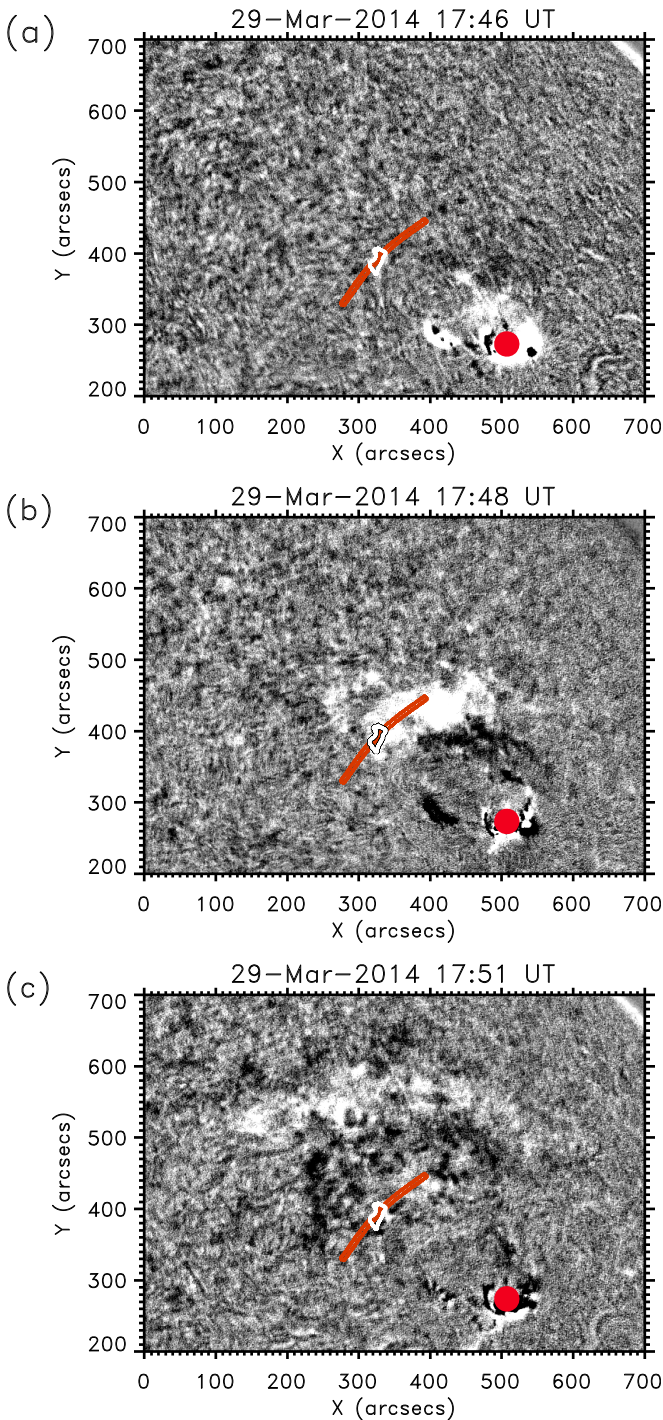


Figure 11. Running difference $H\alpha$ images showing the propagating Moreton wave at selected times. In all panels the filament equilibrium position is outlined by a white contour, the slit is marked by a red arc, and the averaged flare position is marked by a red dot. (a) 17:46 UT, shortly after the wave was generated at the flaring region. (b) 17:48 UT, when the wave (white patch) reached the filament. (c) 17:51 UT, as the wave (white arc) continued to expand and travel northward.

very complex motions prior to and during the passage of the wave through the filament.

Before the oscillations were triggered at 17:47 UT, the filament reached velocities greater than 5 km s^{-1} , but this motion was not periodic (Figure 13(c)). The oscillation velocity peaked at 18:00 UT; after $\sim 18:23$ UT, the measured velocity was very well fitted by the derivative of Equation (2), yielding

a peak amplitude $V = 19.3 \pm 2.3 \text{ km s}^{-1}$, a peak displacement $A = 11 \pm 1 \text{ Mm}$, period $P = 58 \pm 1$ minutes, damping time $\tau = 108 \pm 12$ minutes, and $\tau/P = 1.9 \pm 0.2$. The angle between the motion and the filament spine was $\alpha = 26^\circ$, again consistent with the typical direct measurements of the orientation of the prominence magnetic field relative to the spine (Leroy et al. 1983, 1984; Tandberg-Hanssen 1995; Trujillo Bueno et al. 2002; Casini et al. 2003; López Ariste et al. 2006). Therefore the motion may be aligned with the local magnetic field, and the event is probably a LALO.

9.4. Event 31: SALO with a Very Small Velocity Amplitude

In the survey we also detected oscillations with very small amplitudes of only a few km s^{-1} , below the LAO lower limit of 10 km s^{-1} . Event 31 has the smallest velocity amplitude of the survey: $V = 1.6 \pm 9 \text{ km s}^{-1}$. The filament is an IT, and the oscillation was triggered by a nearby flare. In this example the displacements were too small to be visible in a figure similar to Figure 2. Therefore we refer the reader instead to the movie of this event at the URL: <http://www.iac.es/galeria/mluna/pages/gong-catalogue-of-laos.php>.

Although the displacements are very small in this event, the oscillatory pattern is very clear (Figure 14(a)). Before 17:00 UT the filament appears to be moving, but clear oscillations started at 17:17 UT and ended at 21:06 UT. The displacement appears more or less constant throughout the event (Figure 14(b)). However, the extrapolated oscillation for sometime before and after the fitted oscillation (blue dashed line in Figure 14(b)) does not follow the filament motion, and the oscillation apparently ended without strong damping. In general, the velocity has a large uncertainty for small-amplitude events. In this case, the velocity error is 9 km s^{-1} , much greater than the velocity $V = 1.6 \text{ km s}^{-1}$. Figure 14 exhibits distinct oscillatory motions, so we are probably overestimating the positional errors (see Section 8.1). The displacement was very small ($A = 1 \pm 1 \text{ Mm}$), the oscillation period $P = 77 \pm 4$ minutes, and the damping time $\tau = 662 \pm 1546$ minutes, so the damping was very weak with a large uncertainty (see Table 5). The angle between the slit and the spine $\alpha = 26^\circ$, suggesting that the oscillation was longitudinal.

9.5. Events 145 and 146*: Double Event

In these events, two clear oscillations occurred in the same filament within one observing interval; therefore we labeled them as separate events. In our example, the filament is of the IT type with a curved initial structure (Figure 15(a)). Both oscillations involve motions mainly transverse to the filament spine, with $\alpha = 50^\circ$. A nearby flare, marked by the red dot in the figure, is the most likely trigger. At onset the entire filament was displaced laterally toward the northeast (Figure 15(b)); then after a half period the filament moved to the other side of its equilibrium position (Figure 15(c)). The slit (red outline) is over the region of the filament that oscillated with the largest displacement, which protruded from the rest of the structure.

There were many data gaps, which appear as white vertical bands at the beginning of the time–distance diagram (Figure 16(a)). The first event, 145, oscillated most visibly between 13:31 and 15:33 UT. The oscillation period was $P = 39 \pm 2$ minutes, $V = 14.4 \pm 6.1 \text{ km s}^{-1}$, and $\tau = 48 \pm 13$ minutes (see Table 7), indicating very strong damping with $\tau/P = 1.2 \pm 0.4$. Event 146*, which started at 17:38 UT and

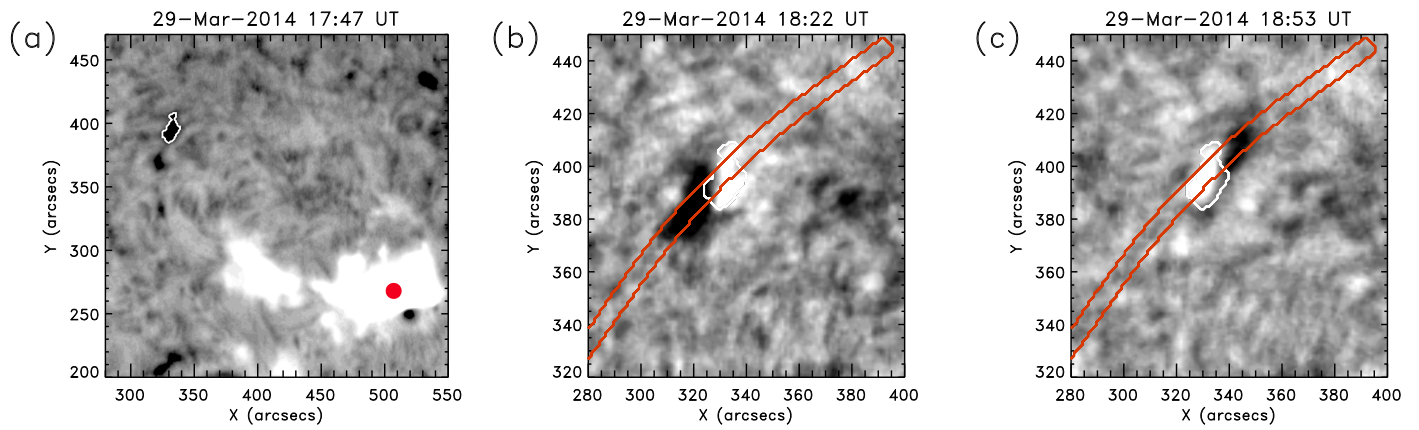


Figure 12. Temporal sequence of the triggering and oscillations in event 91. Panels and annotations are as in Figure 2. (a) $H\alpha$ image of the flaring region and the filament at oscillation onset (17:47 UT). The red dot indicates the approximate position of the flare that produced the Moreton wave that triggered the oscillation. (b) and (c) Running difference $H\alpha$ images of a smaller region centered on the filament. The filament was displaced initially to the southeast (b), and then toward the northwest (c).

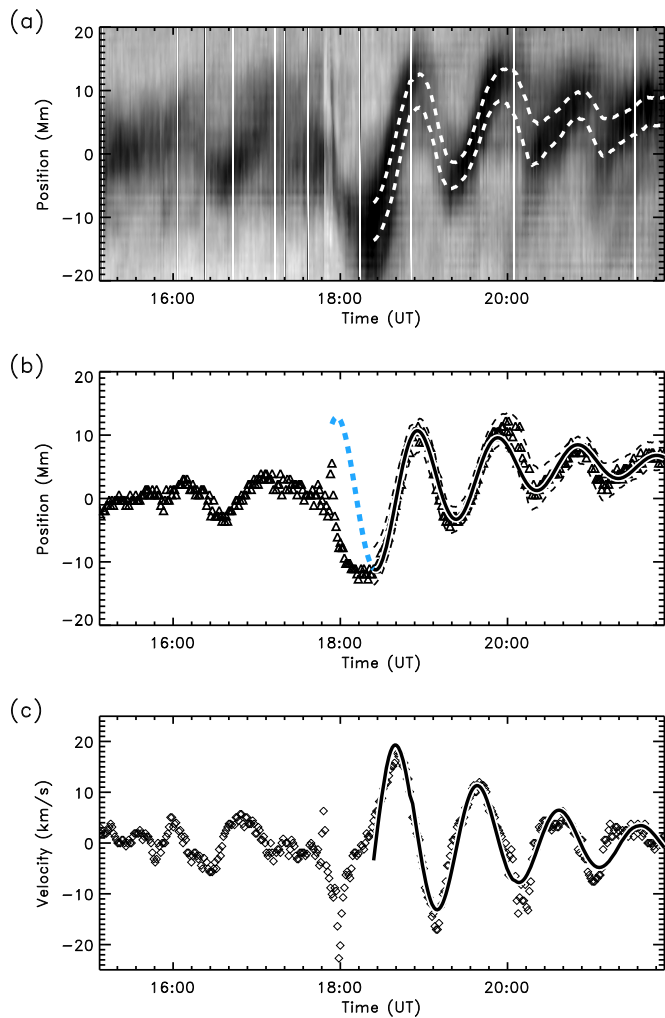


Figure 13. Oscillation diagnostics of event 91. Panels and annotations are as in Figure 4.

ended at 19:20 UT, had $P = 36 \pm 2$ minutes, $V = 3.4 \pm 9.4$, and $\tau = 119 \pm 146$ minutes with $\tau/P = 3.3 \pm 4$. Figure 16(a) leaves the impression that both events were part of a long oscillation starting at 13:31 UT and continuing throughout the temporal sequence. However, the velocity evolution

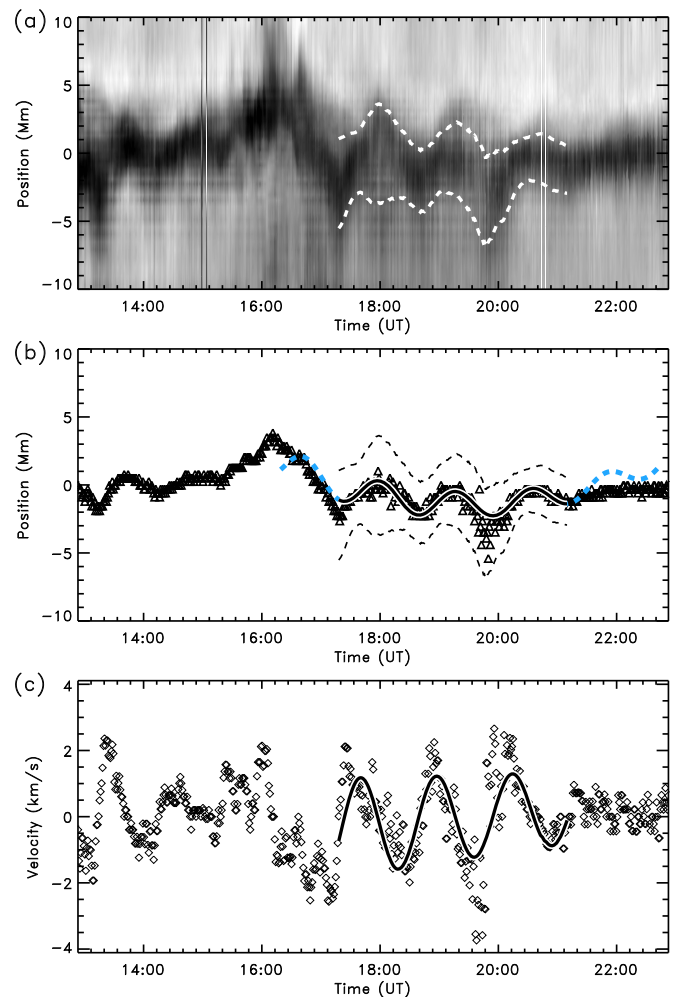


Figure 14. Oscillation diagnostics of event 31. Panels and annotations are as in Figure 4.

demonstrates that case 145 ended at 15:33 UT (Figure 16(c)), followed by an interval of complex oscillation. Event 146* started at 17:38 UT, with a very clear oscillation that was out of phase with previous motions. We conclude that repetitive triggering occurred in this filament.

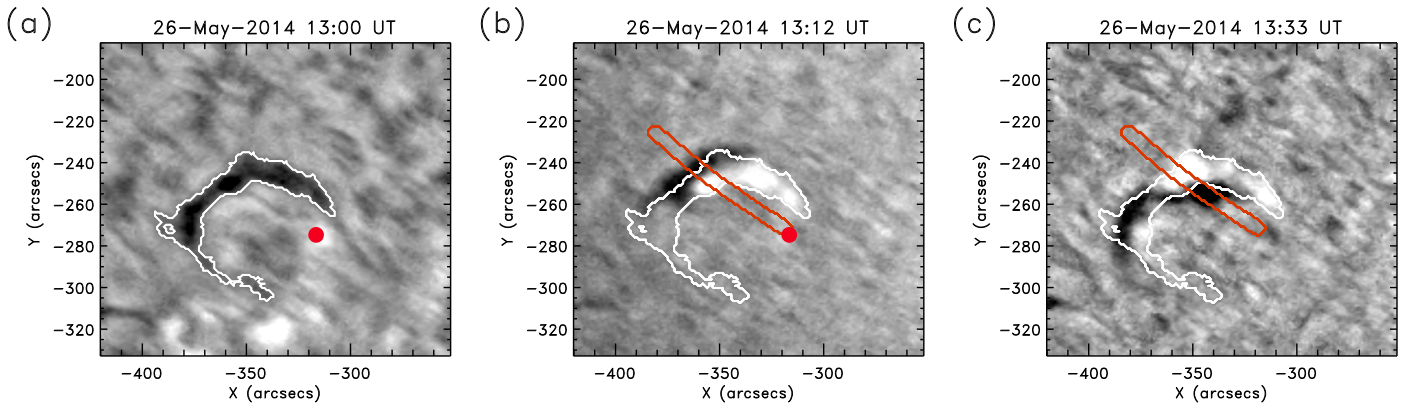


Figure 15. Temporal sequence of the triggering and oscillations in event 145. Panels and annotations are as in Figure 2. In (a) and (b) the red dot indicates the approximate position of the flare that probably triggered the oscillation.

It is interesting that both events had similar periods, suggesting that the filament oscillated with a characteristic frequency of the system (e.g., Hyder 1966). However, the damping times were very different, indicating that either the damping mechanisms were different or the damping efficiency changed between events. The first case had a peak velocity $\sim 14 \text{ km s}^{-1}$, much larger than the second event with $V \sim 3 \text{ km s}^{-1}$. In Section 10.3 we show that the damping time decreases with V for the entire set of events. This nonlinear effect might explain the different damping times for cases 145 and 146*. Both oscillations are very clear in Figure 16, and both fits according to Equation (2) are good. Although the second oscillation continued after 19:20 UT, the extrapolated fitted function (blue dashed line in Figure 16(b)) does not follow the center of the dark band (triangles) well during this interval, probably because the dark band is very light and the signal-to-noise ratio is very low in the time–distance diagram. Event 145 is a transverse LAO with $V = 14.4 \text{ km s}^{-1}$, and 146* is a transverse SAO with $V = 3.4 \text{ km s}^{-1}$ (see Figure 16(c)).

9.6. Event 151 and 152*: Double Event and Amplified Oscillation

Unlike the double event described in the previous section, the cases presented here exhibit very different oscillation periods: $P = 52 \pm 2$ minutes for case 151 and $P = 66 \pm 3$ minutes for case 152*. Figure 17 shows the first stages of event 151; the initial motion is southward, followed by a reversal toward the north. The direction of motion for event 152* is similar to 151. Both events were apparently triggered by nearby flaring (red dot in Figure 17(a)).

Event 151 occurred between 00:00 UT and 3:33 UT (Figure 18(a)). The best-fit solution to the central position tracks the oscillation well, except for a small discrepancy in the last period (Figure 18(b)). The measured and fitted velocities plotted in panel (c) also agree well. The oscillation parameters are $P = 52 \pm 2$ minutes, $\tau = 89 \pm 23$ minutes, and $\tau/P = 1.7 \pm 0.5$ (strong damping). This event is an SAO with $V = 6.8 \pm 5.1 \text{ km s}^{-1}$. In both events $\alpha = 36^\circ$, suggesting longitudinal oscillations.

Figure 18 also shows the unusual oscillation of event 152*, which started at 5:37 UT, increased in amplitude, and ended at 8:53 UT. The best fit agrees well with $s(t)$ between 5:37 and 8:15 UT but not after this interval, suggesting that the plasma

motion of this amplified oscillation is more complex than Equation (2) (Figure 18(b)). The oscillation parameters are $P = 66 \pm 3$ minutes, $\tau = -163 \pm 105$ minutes, and $\tau/P = -2.5 \pm 2$, indicating very strong amplification. The large error in the damping time is probably overestimated, because the fitted function agrees very well with the oscillation. The fitted maximum velocity amplitude is $V = 4.0 \pm 7.8 \text{ km s}^{-1}$, but the measured velocity reached a maximum of 14 km s^{-1} at 08:40 UT. Later $H\alpha$ data reveal that the oscillation ceased and the filament became stationary again. Similar behavior was found by Molowny-Horas et al. (1999) for an amplified filament oscillation.

In order to amplify the oscillation, the cool plasma must gain energy. Recently Zhou et al. (2017) and Zhang et al. (2017b) found LALOs with an amplified oscillation followed by a damped phase, which they explain as a beating phenomenon between two interacting oscillators (see, e.g., Luna et al. 2006, 2008). In this scenario the oscillations of two regions of the filament are coupled: an active oscillator that transfers energy to the other part of the filament (the passive oscillator). The passive oscillator gains energy with time, so its oscillation is amplified, while the active portion loses energy, reducing its amplitude. The section of the filament oscillating in event 152* should be the passive oscillator because it is gaining energy. However, the active oscillator should be the other region of the filament, but it does not oscillate with a larger amplitude. Therefore this hypothesis does not explain events 151 and 152*. Ballester et al. (2016) found that cooling the prominence plasma could amplify its oscillations, but we cannot test this hypothesis for lack of relevant temperature diagnostics. Alternatively, repetitive nearby flares could produce both oscillation events and possibly amplify the second. The $H\alpha$ data shows flaring activity close to the filament (Figure 17(a)). In this situation the amplified oscillation would be driven by external forcing, which could explain why the period is different from that of the non-amplified previous event.

9.7. Events 107 and 108*: Double Event with Amplified Oscillation and Eruption

This double event is similar to that discussed in Section 9.5—a damped oscillation (case 107) immediately followed by an amplified oscillation (case 108*)—but with a final eruption. Both events occurred in the same IT filament, and both events were triggered by flaring in an AR north of the filament

Table 6
Same as Table 5 for Events 61–120

#	Initial Time	$\alpha(^{\circ})$	P (minutes)	τ (minutes)	τ/P	A (Mm)	V (km s $^{-1}$)
61	2014 Feb 12 17:45	24	73 \pm 3	260 \pm 144	3.6 \pm 2	4 \pm 1	4.6 \pm 3.9
62	2014 Feb 13 18:05	19	48 \pm 1	118 \pm 24	2.5 \pm 0.5	10 \pm 2	20.9 \pm 4.2
63	2014 Feb 13 20:39	2	103 \pm 1	175 \pm 12	1.7 \pm 0.1	47 \pm 2	48.5 \pm 2.4
64	2014 Feb 14 08:38	21	56 \pm 1	79 \pm 6	1.4 \pm 0.1	31 \pm 2	52.1 \pm 3.7
65	2014 Feb 14 20:06	60	63 \pm 3	−40 \pm 7	−0.6 \pm 0.1	10 \pm 1	17.0 \pm 11.5
66	2014 Feb 16 17:26	37	40 \pm 2	188 \pm 255	4.7 \pm 7	2 \pm 2	6.7 \pm 11.9
67	2014 Feb 17 02:42	12	92 \pm 3	122 \pm 18	1.3 \pm 0.2	9 \pm 1	14.9 \pm 3.1
68	2014 Feb 17 19:59	25	39 \pm 3	117 \pm 149	3.0 \pm 4	3 \pm 2	8.1 \pm 11.6
69	2014 Feb 19 15:38	16	76 \pm 2	88 \pm 13	1.2 \pm 0.2	20 \pm 3	28.7 \pm 6.1
70	2014 Feb 22 09:04	23	51 \pm 2	51 \pm 13	1.0 \pm 0.3	10 \pm 3	25.7 \pm 8.2
71	2014 Feb 23 16:04	26	34 \pm 1	42 \pm 8	1.2 \pm 0.2	11 \pm 2	34.7 \pm 6.1
72	2014 Feb 24 15:03	22	73 \pm 1	416 \pm 127	5.7 \pm 2	7 \pm 1	10.5 \pm 2.9
73	2014 Feb 24 19:13	20	54 \pm 2	155 \pm 81	2.9 \pm 2	5 \pm 2	9.3 \pm 7.9
74	2014 Feb 25 15:23	50	65 \pm 2	102 \pm 21	1.6 \pm 0.3	5 \pm 1	9.8 \pm 3.5
75	2014 Feb 25 15:28	16	65 \pm 3	80 \pm 27	1.2 \pm 0.5	4 \pm 2	8.9 \pm 6.5
76	2014 Feb 25 12:37	15	78 \pm 2	3 \pm 1	4.8 \pm 3.3
77	2014 Feb 27 09:48	7	57 \pm 1	75 \pm 8	1.3 \pm 0.2	29 \pm 3	54.6 \pm 6.3
78	2014 Feb 27 15:59	34	53 \pm 2	136 \pm 90	2.6 \pm 2	4 \pm 2	9.6 \pm 6.2
79*	2014 Feb 27 19:41	34	51 \pm 1	87 \pm 20	1.7 \pm 0.4	7 \pm 2	18.9 \pm 5.9
80	2014 Feb 28 12:08	10	109 \pm 2	312 \pm 106	2.9 \pm 1	9 \pm 2	9.6 \pm 2.8
81	2014 Mar 7 16:44	21	49 \pm 1	423 \pm 345	8.6 \pm 7	4 \pm 1	9.5 \pm 3.7
82	2014 Mar 12 09:02	1	105 \pm 10	115 \pm 52	1.1 \pm 0.6	12 \pm 3	20.5 \pm 11.1
83	2014 Mar 14 13:31	35	70 \pm 2	89 \pm 14	1.3 \pm 0.2	8 \pm 2	14.4 \pm 3.0
84	2014 Mar 16 03:31	37	46 \pm 1	74 \pm 15	1.6 \pm 0.4	11 \pm 2	26.4 \pm 5.9
85	2014 Mar 20 16:02	19	93 \pm 2	73 \pm 8	0.8 \pm 0.09	16 \pm 2	21.8 \pm 3.8
86	2014 Mar 21 17:23	7	61 \pm 2	89 \pm 25	1.5 \pm 0.4	13 \pm 2	19.6 \pm 5.1
87	2014 Mar 23 16:05	22	76 \pm 1	71 \pm 5	0.9 \pm 0.07	16 \pm 2	29.6 \pm 3.5
88	2014 Mar 24 19:17	29	44 \pm 2	50 \pm 8	1.2 \pm 0.2	7 \pm 1	16.0 \pm 4.0
89*	2014 Mar 24 20:57	29	38 \pm 2	251 \pm 269	6.6 \pm 7	1 \pm 1	3.8 \pm 6.5
90	2014 Mar 28 17:52	0	81 \pm 3	135 \pm 32	1.7 \pm 0.4	8 \pm 2	10.8 \pm 3.9
91	2014 Mar 29 18:23	26	58 \pm 1	108 \pm 12	1.9 \pm 0.2	11 \pm 1	19.3 \pm 2.3
92	2014 Mar 29 15:50	12	87 \pm 2	139 \pm 20	1.6 \pm 0.3	31 \pm 3	38.8 \pm 4.4
93	2014 Mar 30 03:53	10	59 \pm 5	8 \pm 2	15.7 \pm 9.2
94	2014 Mar 31 16:11	30	51 \pm 2	43 \pm 11	0.8 \pm 0.2	6 \pm 2	18.9 \pm 7.0
95*	2014 Mar 31 19:38	30	58 \pm 1	325 \pm 62	5.6 \pm 1	17 \pm 2	32.5 \pm 2.5
96	2014 Apr 7 21:46	19	41 \pm 1	70 \pm 9	1.7 \pm 0.2	10 \pm 1	24.2 \pm 2.8
97	2014 Apr 9 11:21	33	56 \pm 1	71 \pm 11	1.3 \pm 0.2	10 \pm 2	24.9 \pm 4.5
98	2014 Apr 9 18:19	29	51 \pm 4	103 \pm 110	2.0 \pm 2	3 \pm 2	6.8 \pm 10.6
99	2014 Apr 10 06:14	20	52 \pm 1	94 \pm 13	1.8 \pm 0.3	8 \pm 1	13.7 \pm 2.9
100	2014 Apr 14 12:16	7	50 \pm 1	53 \pm 4	1.0 \pm 0.09	20 \pm 2	32.4 \pm 2.7
101	2014 Apr 17 05:20	25	52 \pm 1	83 \pm 8	1.6 \pm 0.2	9 \pm 1	22.8 \pm 2.8
102	2014 Apr 17 02:21	3	92 \pm 2	179 \pm 35	1.9 \pm 0.4	8 \pm 1	9.7 \pm 2.4
103	2014 Apr 17 17:41	39	56 \pm 1	61 \pm 7	1.1 \pm 0.1	11 \pm 2	25.5 \pm 3.7
104	2014 Apr 17 18:38	8	73 \pm 4	1 \pm 1	2.1 \pm 7.4
105	2014 Apr 19 02:57	0	59 \pm 2	118 \pm 34	2.0 \pm 0.6	9 \pm 2	12.9 \pm 4.4
106	2014 Apr 19 12:44	26	65 \pm 1	114 \pm 20	1.8 \pm 0.3	8 \pm 2	15.0 \pm 4.3
107	2014 Apr 21 18:20	20	50 \pm 1	155 \pm 34	3.1 \pm 0.7	4 \pm 1	6.6 \pm 2.2
108*	2014 Apr 21 21:29	20	40 \pm 3	−97 \pm 70	−2.4 \pm 2	2 \pm 1	5.6 \pm 9.3
109	2014 Apr 22 12:17	11	61 \pm 1	110 \pm 19	1.8 \pm 0.3	5 \pm 1	8.5 \pm 3.4
110	2014 Apr 23 14:32	26	51 \pm 4	45 \pm 15	0.9 \pm 0.3	7 \pm 2	10.5 \pm 7.4
111	2014 Apr 24 04:04	16	43 \pm 1	232 \pm 42	5.3 \pm 0.1	8 \pm 1	18.5 \pm 3.3
112	2014 Apr 24 10:53	21	41 \pm 2	37 \pm 6	0.9 \pm 0.1	13 \pm 2	27.7 \pm 6.2
113	2014 Apr 25 03:17	16	58 \pm 2	276 \pm 189	4.7 \pm 3	2 \pm 1	3.0 \pm 6.4
114	2014 Apr 26 12:40	54	47 \pm 3	55 \pm 21	1.2 \pm 0.5	6 \pm 2	11.0 \pm 8.7
115	2014 May 1 17:40	8	70 \pm 1	78 \pm 4	1.1 \pm 0.06	25 \pm 2	48.4 \pm 2.8
116	2014 May 1 16:17	23	52 \pm 1	218 \pm 103	4.2 \pm 2	3 \pm 1	6.4 \pm 4.9
117	2014 May 1 03:08	81	52 \pm 2	125 \pm 44	2.4 \pm 0.9	2 \pm 1	3.3 \pm 4.8
118	2014 May 2 02:17	8	76 \pm 1	377 \pm 144	5.0 \pm 2	6 \pm 1	7.0 \pm 2.4
119*	2014 May 2 09:08	8	72 \pm 5	110 \pm 89	1.5 \pm 1	5 \pm 3	9.3 \pm 9.8
120	2014 May 2 11:04	48	50 \pm 4	51 \pm 19	1.0 \pm 0.4	4 \pm 2	6.1 \pm 8.6

(Figure 19(a)). For the first event, $P = 50 \pm 1$ minutes, $V = 6.6 \pm 2.2$ km s $^{-1}$, and $\tau/P = 3.1 \pm 0.7$; for the second event, $P = 40 \pm 3$ minutes, $V = 5.6 \pm 9.3$ km s $^{-1}$, and $\tau/P =$

-2.4 ± 2.0 . Both events are SAOs with $\alpha = 20^{\circ}$, denoting longitudinal polarization. As in events 151 and 152*, the periods are different.

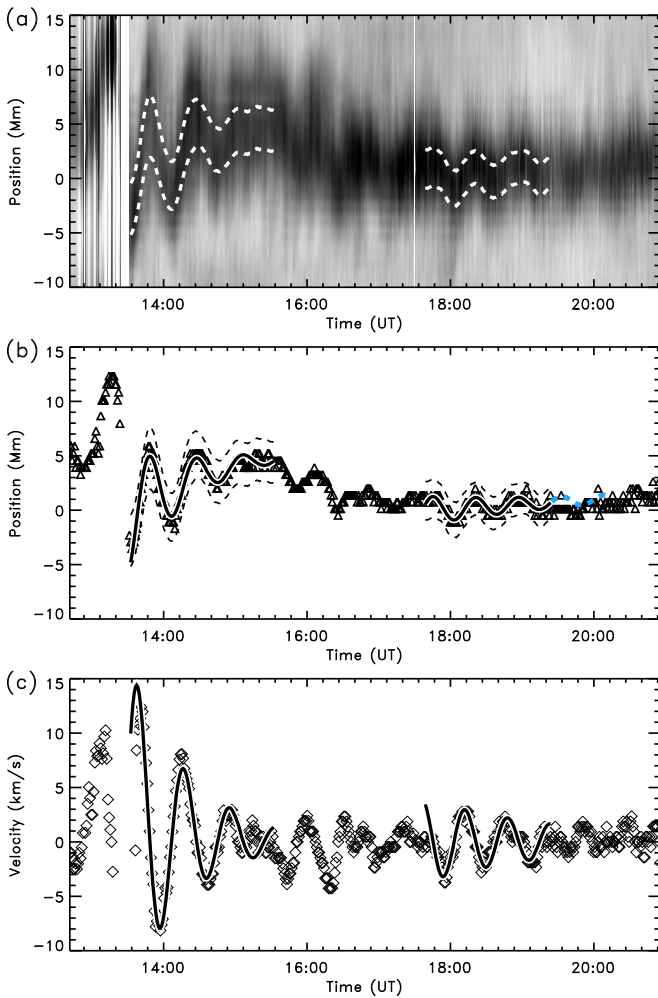


Figure 16. Oscillation diagnostics of events 145 and 146*. Panels are as in Figure 4.

Simultaneous with the oscillation onset for event 107, a white spot appeared north of the filament (marked with a white arrow in Figure 19(a)) and continued almost to the end of event 107. Because the slit in Figures 19(b), (c) passes over the white spot, we can also see this brightening in the resulting time–distance diagram (Figure 20(a)). Base difference images show the maximum elongation of the cool plasma for event 107 (Figure 19(b)) and for event 108* (Figure 19(c)). At the end of event 108*, the prominence erupts ($\sim 23:20$ UT, not shown). The white spot that appeared north of the filament appears as a bright region at the top of the dark band in Figure 20(a). This bright emission apparently followed the motion of the threads from 18:20 to 21:20 UT (end of event 107).

As with events 145 and 146*, the oscillation seems to be continuous between 18:20 UT and 23:26 UT. However, the event 107 and 108* oscillations differ significantly in phase, period, and damping time. Figure 20(b) shows this discrepancy clearly: one fit (Equation (2)) is very good in the first event and another is good in the second, except at the end of the event when the motion was obviously affected by the eruption. The differences between two events are equally evident in the measured velocities (Figure 20(c)). Before 18:20 UT the motions were small and disorganized, while after this time the damped oscillation is very clear. At 23:26 UT the period changed and the oscillation started to grow, ending in an eruption.

The main difference between events 107–108* and the amplified oscillation of Section 9.6 is that the filament erupts. However, similar explanations might apply for the amplification. The potential relationship between the amplified oscillation and the eruption is an intriguing topic for further study.

10. Statistics

The catalog consists of 196 oscillation events, which we found by analyzing 6 months of GONG data in cycle 24 (see Tables 1–8). In about 43% of the cases, we identified the apparent trigger of the oscillation: 72 events were triggered by flares, 11 by PEs, 1 by a jet, and 1 by an MW. However, in 111 cases the triggering agent was not identified. In 9 cases the filament erupted during the temporal range analyzed.

As discussed in Section 1, we classified the oscillations according to their maximum velocity amplitude as SAOs ($V < 10 \text{ km s}^{-1}$) and LAOs ($V > 10 \text{ km s}^{-1}$). Of the 196 oscillation events, there are 106 SAOs and 90 LAOs. Over the 6 months of the survey, this averages to one oscillation event per day on the visible solar disk. The occurrence rate of one LAO event every 2 days implies that LAOs are a common phenomena on the Sun, in contrast to previous statements that LAOs are scarce (e.g., Tripathi et al. 2009). We also found a similar rate for SAOs.

The data presented in the catalog enabled us to search for possible dependencies between pairs of filament and oscillation parameters: the velocity amplitude (V), oscillation period (P), damping time (τ), damping time per period (τ/P), displacement (A), and angle between the proper motion and the filament spine (α). We also computed the Pearson correlation matrix (Neter et al. 1993) using the IDL subroutine *correlate.pro*. The matrix elements are the correlations between pairs of parameters, and range from -1 to 1 . A linear correlation between two parameters yields an associated matrix element close to 1 (or -1). Although we found that the values of the matrix are small, in general, we will discuss those pairs of parameters whose correlations or lack thereof are interesting. Figures 21–23 show scatter plots of some pairs of these parameters. In Figure 21 the scatter plots of the period, P , versus the other parameters are displayed in six panels (a–f). Figure 22 shows the damping parameters, τ or τ/P , versus V and α (panels a–e). Figure 23 plots several parameters versus solar latitude of the filament. In these scatter plots, the LAOs and SAOs are plotted with circles and squares, respectively.

10.1. Velocity Amplitude, V

In the survey we found velocity amplitudes from a few km s^{-1} to 55 km s^{-1} (see Tables 5–8). Histograms of the velocity distribution for all events and the distribution according to filament type are plotted in Figures 24(a) and (d), respectively. The vertical dotted line separates LAOs ($V > 10 \text{ km s}^{-1}$) from SAOs ($V < 10 \text{ km s}^{-1}$). The total number of LAO events decreases with the velocity amplitude, as expected: more energetic events are less frequent than less energetic ones. The velocity ranges for all filament types (AR—red, IT—green, and QS—blue) are similar (Figure 24(d)), indicating that all types of filaments can support both SAOs and LAOs. The velocity distribution for each filament type follows the same trend as the total distribution, except for AR filaments. The apparent rollover in the AR filament distribution below 5 km s^{-1} probably reflects the difficulty in detecting

Table 7
Same as Table 5 for Events 121–180

#	Initial Time	$\alpha(^{\circ})$	P (minutes)	τ (minutes)	τ/P	A (Mm)	V (km s $^{-1}$)
121	2014 May 5 16:13	15	35 \pm 3	26 \pm 8	0.7 \pm 0.3	6 \pm 2	14.2 \pm 9.1
122	2014 May 10 08:01	18	81 \pm 3	198 \pm 104	2.4 \pm 1	3 \pm 1	3.7 \pm 5.8
123	2014 May 10 09:14	72	69 \pm 3	119 \pm 58	1.7 \pm 0.9	3 \pm 2	4.6 \pm 6.5
124	2014 May 11 18:47	9	64 \pm 3	46 \pm 8	0.7 \pm 0.2	18 \pm 3	24.0 \pm 5.8
125	2014 May 12 02:40	18	65 \pm 6	86 \pm 52	1.3 \pm 0.9	4 \pm 2	5.3 \pm 9.1
126	2014 May 12 01:19	31	88 \pm 2	212 \pm 55	2.4 \pm 0.7	8 \pm 2	12.3 \pm 3.3
127	2014 May 12 06:20	21	32 \pm 2	34 \pm 9	1.1 \pm 0.3	9 \pm 3	25.0 \pm 9.1
128	2014 May 12 08:22	7	55 \pm 2	123 \pm 35	2.2 \pm 0.7	5 \pm 1	8.4 \pm 4.0
129	2014 May 12 01:26	15	43 \pm 2	50 \pm 16	1.2 \pm 0.4	3 \pm 1	8.0 \pm 5.8
130	2014 May 13 18:26	16	50 \pm 3	72 \pm 25	1.4 \pm 0.5	4 \pm 1	6.8 \pm 5.6
131	2014 May 13 14:46	74	77 \pm 2	185 \pm 83	2.4 \pm 1	2 \pm 1	2.4 \pm 3.5
132	2014 May 14 07:13	87	99 \pm 5	227 \pm 138	2.3 \pm 1	4 \pm 2	3.6 \pm 5.6
133	2014 May 15 18:25	44	76 \pm 2	87 \pm 12	1.1 \pm 0.2	8 \pm 1	12.9 \pm 2.7
134	2014 May 16 02:25	35	85 \pm 5	−224 \pm 195	−2.6 \pm 2	2 \pm 1	4.5 \pm 9.0
135	2014 May 16 11:49	7	50 \pm 1	11 \pm 1	24.7 \pm 3.2
136	2014 May 17 02:37	2	59 \pm 3	218 \pm 219	3.7 \pm 4	3 \pm 2	5.1 \pm 7.4
137	2014 May 17 10:35	20	58 \pm 2	78 \pm 12	1.4 \pm 0.2	19 \pm 2	29.5 \pm 5.1
138	2014 May 18 18:22	38	57 \pm 1	49 \pm 6	0.9 \pm 0.1	9 \pm 2	23.5 \pm 4.3
139	2014 May 23 15:06	48	56 \pm 2	179 \pm 111	3.2 \pm 2	2 \pm 1	4.1 \pm 5.4
140	2014 May 23 14:58	18	48 \pm 2	82 \pm 20	1.7 \pm 0.4	8 \pm 2	13.8 \pm 5.2
141	2014 May 23 14:14	4	48 \pm 3	213 \pm 216	4.4 \pm 5	2 \pm 1	4.0 \pm 8.5
142	2014 May 23 18:01	37	46 \pm 2	32 \pm 7	0.7 \pm 0.2	6 \pm 2	20.1 \pm 7.2
143	2014 May 26 02:38	13	62 \pm 2	53 \pm 6	0.9 \pm 0.01	15 \pm 2	21.2 \pm 2.8
144	2014 May 26 17:52	62	53 \pm 2	180 \pm 145	3.4 \pm 3	3 \pm 1	6.9 \pm 6.2
145	2014 May 26 13:31	50	39 \pm 2	48 \pm 13	1.2 \pm 0.4	5 \pm 2	14.4 \pm 6.1
146*	2014 May 26 17:38	50	36 \pm 2	119 \pm 146	3.3 \pm 4	1 \pm 1	3.4 \pm 9.4
147	2014 May 27 03:16	1	70 \pm 2	444 \pm 385	6.3 \pm 6	3 \pm 1	4.5 \pm 5.4
148	2014 May 27 09:16	36	34 \pm 3	40 \pm 22	1.2 \pm 0.7	2 \pm 1	4.8 \pm 10.0
149	2014 May 28 00:34	42	75 \pm 6	467 \pm 1263	6.2 \pm 20	2 \pm 2	3.5 \pm 9.2
150	2014 May 29 01:16	27	42 \pm 1	86 \pm 13	2.1 \pm 0.3	8 \pm 1	21.2 \pm 4.3
151	2014 May 30 00:01	36	52 \pm 2	89 \pm 23	1.7 \pm 0.5	4 \pm 1	6.8 \pm 5.1
152*	2014 May 30 05:37	36	66 \pm 3	−163 \pm 105	−2.5 \pm 2	3 \pm 1	4.0 \pm 7.8
153	2014 May 30 11:43	36	45 \pm 12	1 \pm 3	4.1 \pm 30.4
154*	2014 May 30 13:42	36	37 \pm 3	49 \pm 25	1.3 \pm 0.7	7 \pm 4	17.2 \pm 15.4
155	2014 Jun 1 02:06	32	32 \pm 13	101 \pm 859	3.1 \pm 30	0 \pm 2	1.7 \pm 52.6
156	2014 Jun 2 07:05	51	73 \pm 3	−291 \pm 236	−4.0 \pm 3	2 \pm 1	3.6 \pm 5.9
157	2014 Jun 2 18:26	14	84 \pm 2	2 \pm 1	2.4 \pm 3.9
158	2014 Jun 3 02:33	19	74 \pm 7	557 \pm 2260	7.5 \pm 30	1 \pm 1	1.2 \pm 13.5
159	2014 Jun 4 17:30	33	79 \pm 2	155 \pm 29	2.0 \pm 0.4	6 \pm 1	6.6 \pm 2.6
160	2014 Jun 5 10:20	50	60 \pm 1	272 \pm 73	4.6 \pm 1	2 \pm 1	3.6 \pm 3.2
161	2014 Jun 5 19:57	16	49 \pm 2	51 \pm 13	1.1 \pm 0.3	5 \pm 2	10.3 \pm 6.1
162	2014 Jun 6 10:46	2	48 \pm 3	2 \pm 1	3.9 \pm 7.0
163	2014 Jun 7 00:36	64	45 \pm 3	33 \pm 9	0.7 \pm 0.2	9 \pm 3	16.2 \pm 13.1
164	2014 Jun 7 07:26	42	52 \pm 3	106 \pm 62	2.1 \pm 1	3 \pm 1	5.9 \pm 6.4
165*	2014 Jun 7 11:26	42	58 \pm 2	123 \pm 39	2.1 \pm 0.7	5 \pm 2	9.1 \pm 4.9
166	2014 Jun 8 10:17	13	56 \pm 5	46 \pm 20	0.8 \pm 0.4	5 \pm 4	11.3 \pm 11.9
167	2014 Jun 8 16:55	29	55 \pm 3	193 \pm 167	3.5 \pm 3	2 \pm 1	3.6 \pm 8.0
168	2014 Jun 9 07:32	34	47 \pm 2	64 \pm 16	1.3 \pm 0.4	6 \pm 2	11.7 \pm 5.2
169*	2014 Jun 9 11:55	34	40 \pm 1	84 \pm 21	2.1 \pm 0.5	6 \pm 1	12.4 \pm 3.5
170	2014 Jun 9 14:46	40	58 \pm 4	1 \pm 1	2.2 \pm 17.5
171	2014 Jun 9 09:34	1	62 \pm 3	−202 \pm 226	−3.2 \pm 4	1 \pm 1	2.6 \pm 9.3
172*	2014 Jun 9 13:59	1	57 \pm 2	280 \pm 189	4.9 \pm 3	3 \pm 1	5.5 \pm 5.3
173	2014 Jun 10 18:19	35	36 \pm 1	84 \pm 20	2.4 \pm 0.6	6 \pm 1	17.3 \pm 4.8
174	2014 Jun 12 00:01	20	63 \pm 1	275 \pm 118	4.4 \pm 2	5 \pm 1	9.9 \pm 3.3
175*	2014 Jun 12 04:31	20	45 \pm 1	207 \pm 134	4.6 \pm 3	1 \pm 1	2.8 \pm 5.1
176	2014 Jun 12 01:50	21	67 \pm 3	3 \pm 1	5.1 \pm 5.7
177*	2014 Jun 12 05:37	21	54 \pm 3	56 \pm 35	1.0 \pm 0.7	13 \pm 5	15.1 \pm 9.5
178	2014 Jun 12 00:30	47	67 \pm 2	118 \pm 31	1.8 \pm 0.5	4 \pm 1	5.3 \pm 5.1
179	2014 Jun 12 13:11	13	52 \pm 1	57 \pm 8	1.1 \pm 0.2	10 \pm 2	22.1 \pm 5.0
180*	2014 Jun 12 14:10	13	51 \pm 1	142 \pm 48	2.8 \pm 0.1	4 \pm 1	8.3 \pm 4.1

small filaments and small-amplitude events by visual inspection only, implying that we have underestimated the number of SAOs.

The histograms also do not distinguish two separate populations associated with large- and small-amplitude oscillations, regardless of the choice of LAO threshold (i.e., 10 km s $^{-1}$

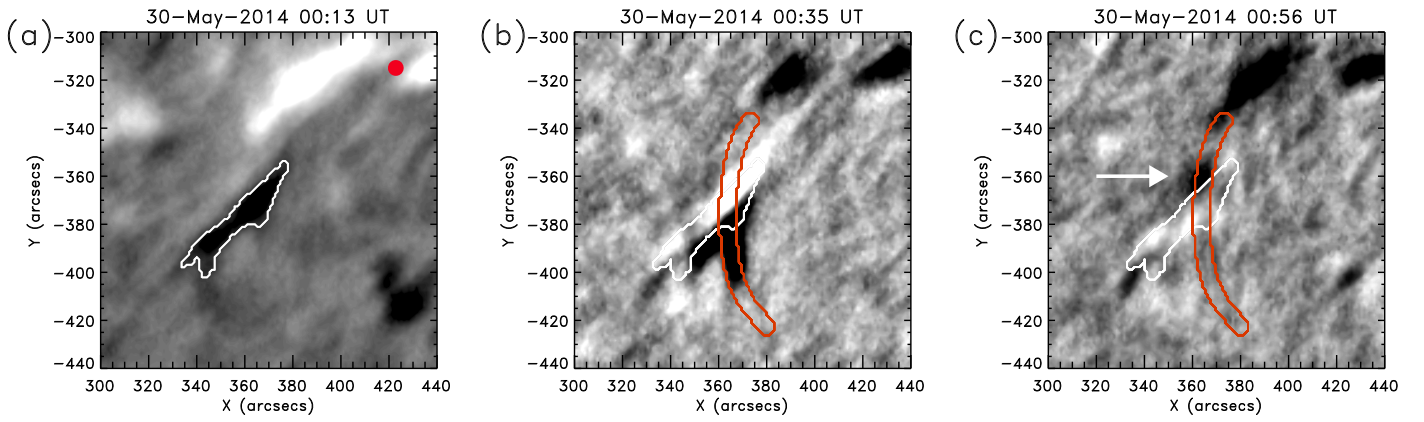


Figure 17. Temporal sequence of the triggering and oscillations in events 151 and 152*. Panels and annotations are as in Figure 2. In (c) the white arrow points to the part of the prominence that oscillates.

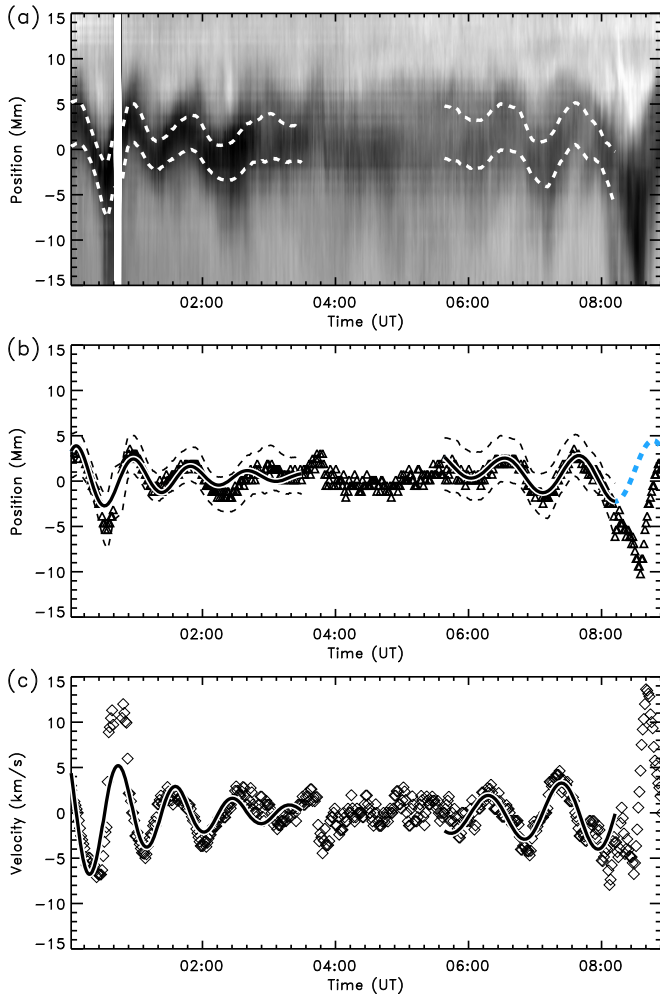


Figure 18. Oscillation diagnostics of events 151 and 152*. Panels are as in Figure 4.

or 20 km s^{-1}). Additionally, 32 of the 106 SAOs were clearly triggered by an identified energetic disturbance. These contradict the idea that the LAOs and SAOs have a different nature and are triggered by different mechanisms (Oliver & Ballester 2002; Arregui et al. 2012).

The P - V scatter plot (Figure 21(a)) and the small correlation P - V value reveal no dependence of the velocity on the period, neither for all events nor for different filament types. In contrast,

the V - α scatter plot (Figure 22(a)) shows a clear pattern: the V range decreases with α , and the V values drop sharply for events with α beyond 40° . This tendency leads to no LAOs for $\alpha > 65^\circ$. The two populations can be also distinguished in the A - α scatter plot of Figure 22(b), as we will discuss in Section 10.4. The evident correlation between velocity amplitude and damping time will be discussed in Section 10.3.

10.2. Period, P

The period reflects the restoring force and the underlying physics of the oscillation. The period values range from 30 to 110 minutes for the total population, with a mean value of 58 minutes, a standard deviation of 15 minutes, and a clear peak centered at ~ 58 minutes (Figure 24(b)). The period distributions for LAOs (striped) and SAOs (shaded) have mean values and standard deviations comparable to those of the P distribution for all events. This indicates that SAOs and LAOs are not two distinct populations of events with respect to their periods.

The period distributions for the three filament types do not differ significantly from each other or from the total distribution (Figure 24(e)). For IT filaments, the mean period is $56 \text{ minutes} \pm 14 \text{ minutes}$; the distribution for AR filaments peaks at $57 \pm 16 \text{ minutes}$; the mean period for QS filaments is $62 \pm 17 \text{ minutes}$ with a long-period tail extending to 110 minutes. If LAOs were nonlinear, as discussed in Section 1, the period could depend on V or A . However, Figures 21(a) and (b), together with the negligible P - V and P - A correlation elements, demonstrate that P depends on neither V nor A for the cataloged events.

Many theoretical models of MHD modes in filaments predict a relationship between the oscillation period and the filament length or width (see the review by Arregui et al. 2012). To test this hypothesis, we plotted the oscillation period as a function of length L and width W in Figures 21(c) and (d), respectively. We found no correlation between P and L for all types. Although the period is not correlated with W for AR and IT filaments, QS filament periods tend to increase with W . The correlation element is relatively large, 0.74, and the linear P - W relationship is

$$P_{\text{QS}} = 23.4 \pm 0.4 + (2.31 \pm 0.02)W_{\text{QS}}, \quad (3)$$

where P_{QS} is in minutes and the errors in the period have been considered. The general tendency is for wider QS filaments to oscillate with longer periods than narrower prominences.

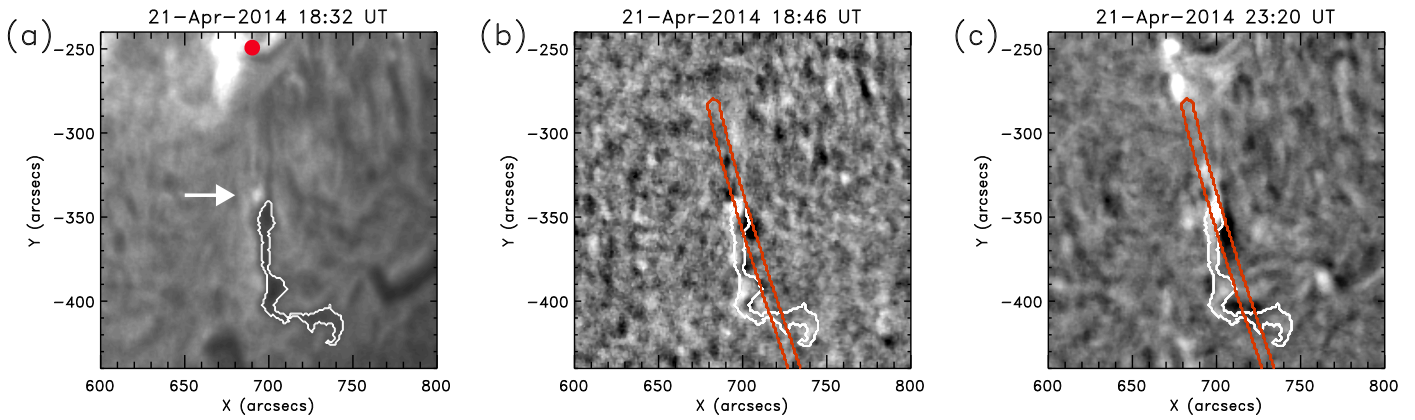


Figure 19. Temporal sequence of the triggering and oscillations in events 107 and 108*. Panels and annotations are as in Figure 2.

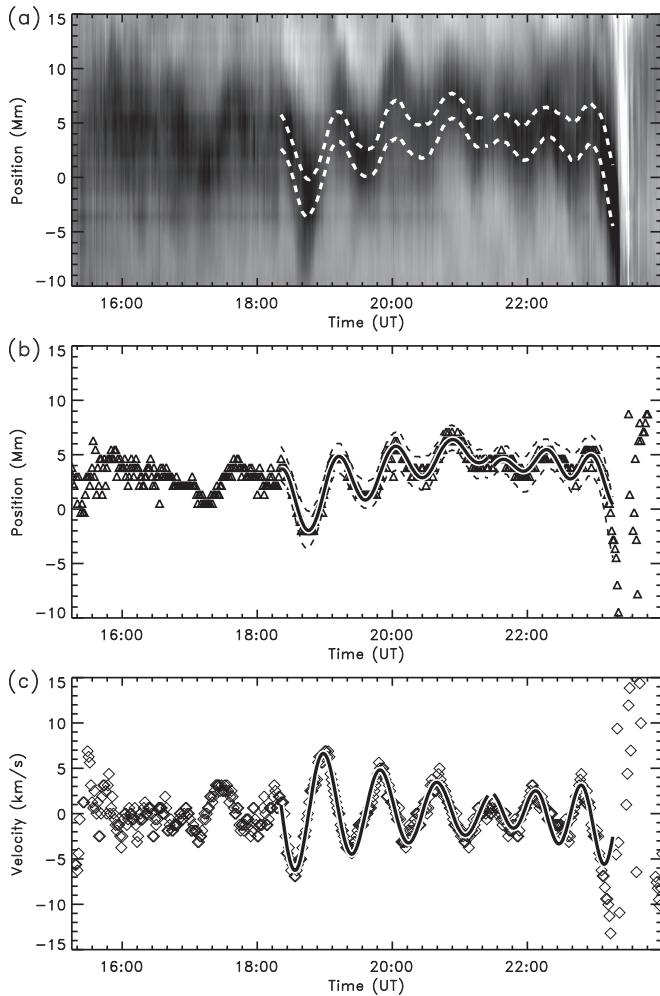


Figure 20. Oscillation diagnostics of events 107 and 108*. Panels and annotations are as in Figure 4.

Figure 21(e) shows that, for angles $\alpha < 70^\circ$, the range of possible periods generally decreases with α . For $\alpha < 20^\circ$ the periods occupy the range from 30 to 110 minutes, whereas for $20^\circ < \alpha < 40^\circ$ the periods range from 30 to 95 minutes, and for $40^\circ < \alpha < 70^\circ$ the range is from 30 to 80 minutes. Only a few cases have $\alpha > 70^\circ$, and some of them do not follow this trend. P decreases gradually with α , so there is a no clear drop in P for $\alpha > 40^\circ$, as we found for V (see Section 10.1).

The decrease of P with α , in conjunction with the sharp decrease in V at $\alpha > 40^\circ$, suggests a connection with the polarization of the oscillations. Theoretical modeling predicts that oscillations along the field have longer periods than transverse oscillations. Wang et al. (2016) and Zhang et al. (2017a) observed simultaneous longitudinal and transverse oscillations in a prominence, and confirmed that the transverse oscillation period was shorter than the longitudinal period. At this point we are tempted to define longitudinal and transverse oscillations according to the V - α results: longitudinal for $\alpha < 40^\circ$ and transverse for $\alpha > 40^\circ$. High-resolution observations reveal that on-disk filaments are composed of many narrow, field-aligned threads oriented at a shallow angle to the spine (e.g., Lin et al. 2005), and often are composed of segments spaced along a common PIL. That is, the spine is not necessarily a coherent, magnetically continuous structure. Transverse oscillations involve coherent movement of the whole magnetic structure or magnetically linked portions thereof, whereas longitudinal oscillations involve individual thread motions at an angle with the spine. In almost all catalog events, only a small fraction of the filament oscillates, suggesting that the local, rather than global, magnetic field is engaged. Further study of individual, well-observed events is needed to resolve whether α is a reliable marker of the boundary between transverse and longitudinal events.

In Section 9.5 we reported two consecutive oscillations in the same filament during the same data sequence. The periods of both events, P and P^* , agreed, suggesting that the common period is the characteristic period of oscillation of the structure (Ramsey & Smith 1966). However, in the cases described in Sections 9.6 and 9.7, P and P^* are clearly different. In Figure 25 the scatter plot of P^* vs. P is shown for all the double events in the catalog. For several cases, the ellipse is inside or close to the region of $P^* \sim P \pm 5$ minutes (the region between the two dotted lines). For these cases, we can reasonably consider the oscillation as a characteristic of the system. The shaded ellipses correspond to the double cases with amplified oscillations, which in some events were probably associated with flaring activity near the filament (see, e.g., Sections 9.6 and 9.7). Thus these oscillations were probably forced and are not characteristic motions. However, more cases exhibit significant differences between P^* and P not associated with oscillation amplification. In almost all of these cases, we found that the substantial period differences were associated with reconfiguration of the filament structure.

Table 8
Same as Table 5 for Events 181–196

#	Initial Time	$\alpha(^{\circ})$	P (minutes)	τ (minutes)	τ/P	A (Mm)	V (km s $^{-1}$)
181	2014 Jun 13 05:38	28	60 \pm 5	1 \pm 1	2.3 \pm 12.9
182	2014 Jun 13 16:37	2	51 \pm 3	245 \pm 353	4.8 \pm 7	1 \pm 1	3.2 \pm 8.5
183	2014 Jun 14 01:44	1	58 \pm 2	493 \pm 673	8.4 \pm 10	1 \pm 1	1.7 \pm 7.4
184	2014 Jun 14 11:38	81	61 \pm 4	249 \pm 313	4.1 \pm 5	1 \pm 1	2.3 \pm 8.5
185	2014 Jun 14 09:46	17	45 \pm 3	2 \pm 2	6.3 \pm 10.0
186	2014 Jun 15 02:37	9	44 \pm 6	1 \pm 1	1.4 \pm 19.3
187*	2014 Jun 15 21:04	9	54 \pm 1	118 \pm 22	2.2 \pm 0.4	7 \pm 1	11.1 \pm 2.6
188	2014 Jun 16 11:43	57	63 \pm 8	237 \pm 356	3.7 \pm 6	2 \pm 1	3.9 \pm 12.6
189	2014 Jun 16 08:50	88	38 \pm 9	125 \pm 501	3.3 \pm 10	0 \pm 1	1.0 \pm 28.2
190*	2014 Jun 16 15:59	88	41 \pm 3	84 \pm 67	2.1 \pm 2	2 \pm 1	3.7 \pm 10.1
191	2014 Jun 17 21:14	20	67 \pm 6	39 \pm 9	0.6 \pm 0.2	4 \pm 2	4.7 \pm 7.4
192	2014 Jun 17 15:50	35	57 \pm 1	162 \pm 51	2.9 \pm 0.9	6 \pm 2	15.0 \pm 4.6
193	2014 Jun 17 09:50	65	42 \pm 1	246 \pm 166	5.8 \pm 4	1 \pm 1	2.8 \pm 4.5
194	2014 Jun 17 12:36	27	51 \pm 2	68 \pm 16	1.3 \pm 0.3	4 \pm 1	9.0 \pm 4.0
195	2014 Jun 19 18:10	14	47 \pm 3	62 \pm 21	1.3 \pm 0.5	3 \pm 1	7.3 \pm 5.1
196	2014 Jun 29 16:21	50	56 \pm 4	61 \pm 28	1.1 \pm 0.6	5 \pm 3	9.4 \pm 10.6

For example, in cases 174–175* and 186–187*, the filament structures change with time, judging from the observed flows along the slit and movements of the equilibrium position of the filament.

10.3. Damping, τ and τ/P

$|\tau/P|$ measures the number of oscillations within the characteristic damping time. The absolute value of τ/P is considered because τ is negative when an oscillation is amplified with time, as discussed in Sections 9.6 and 9.7. A large value of $|\tau/P|$ indicates weak damping, while a small ratio indicates strong damping. The $|\tau/P|$ histogram (Figure 24(c)) for all events extends from 0.6 to 2711 (not shown in the histogram), and peaks at $|\tau/P| = 1.25$. Most events are strongly damped ($|\tau/P| < 3$), and a significant number are very strongly damped ($|\tau/P| < 1$). A value of $|\tau/P| \geq 10$ essentially signifies an undamped oscillation. In contrast with the V and P distributions considered above, the $|\tau/P|$ distributions for SAOs and LAOs clearly differ: the SAO distribution is wide, with a peak close to 1.75, while the LAO distribution is narrower with a peak near 1.25 and scattered points at larger values of $|\tau/P|$. The LAO events ($V > 10$ km s $^{-1}$) are mainly below $|\tau/P| = 3$, while SAOs cover a larger range. The distributions for the three filament types appear similar (Figure 24(f)) to the total $|\tau/P|$ distribution.

Figure 22(c) shows that larger velocity amplitudes are positively correlated with stronger damping, which indicates that the higher-speed oscillations are likely to be nonlinear. The sharp transition in the $|\tau|$ range at $V = 10$ km s $^{-1}$ divides LAOs from SAOs in Figure 22(a), reflecting a distinct boundary between linear and nonlinear oscillations. The scatter plot $|\tau/P|$ – V is not shown but resembles that of Figure 22(a) with the same trend: the damping time $|\tau/P|$ decreases as V increases.

Zhang et al. (2013) found a nonlinear relationship between τ and V in their simulations of prominence mass formation: $\tau \sim V^{-0.3}$. This scaling law (solid black line in Figure 22(c)) is roughly consistent with observed and derived values from our events, suggesting that LAOs may be damped through radiative cooling. In their model, each flux tube supporting a

cool thread has two coronal segments that connect the thread with the chromosphere at both footpoints. The oscillations alternately compress and rarefy both segments, heating or cooling the coronal plasma. The combined density and temperature increases raise the radiative losses, thus damping the oscillations. The Zhang et al. (2013) model predicted that this effect could yield a temperature variation of several hundred thousand Kelvins, which is not observed. An alternative mechanism that can explain strong damping is the mass accretion associated with thermal nonequilibrium (Luna & Karpen 2012; Ruderman & Luna 2016), when evaporated chromospheric plasma continually condenses onto the prominence threads. In this model the damping is not related directly to the oscillation velocity. However, events with larger V are associated with violent events, which could produce increased evaporation and consequently stronger damping. A combination of mass accretion and radiative damping is also possible.

$|\tau/P|$ and dimensions L and W are uncorrelated (the corresponding correlation elements are close to zero), implying that the damping is not related to the prominence size. The building blocks of prominences are cool, elongated threads aligned with the magnetic field, so the damping process is probably associated with the local magnetic or plasma characteristics, and not with the global dimensions of the filament. Similarly, $|\tau/P|$ is uncorrelated with P or A .

The τ/P – α scatter plot (Figure 22(d)) shows a decreased range of τ/P for $\alpha > 40^{\circ}$. This behavior is similar to the V – α (Section 10.1) and the A – α scatter plots, as we will discuss in Section 10.4.

Events 6, 7, 38, 65, 108, 134, 152, 156, and 171 were characterized by amplified oscillations ($\tau < 0$). In Figures 21–23 these cases are marked by symbols surrounded by a big diamond. Cases 6*, 7, 65, 171 are similar to 108* and 152*: an amplified oscillation prior to a filament reconfiguration or eruption. Case 38 is less clear but probably is associated with reconfiguration. The amplification in cases 134 and 156 is not evident in the time–distance diagrams, and might be associated with filament proper motions. These amplified oscillations are very interesting and deserve to be studied in greater depth.

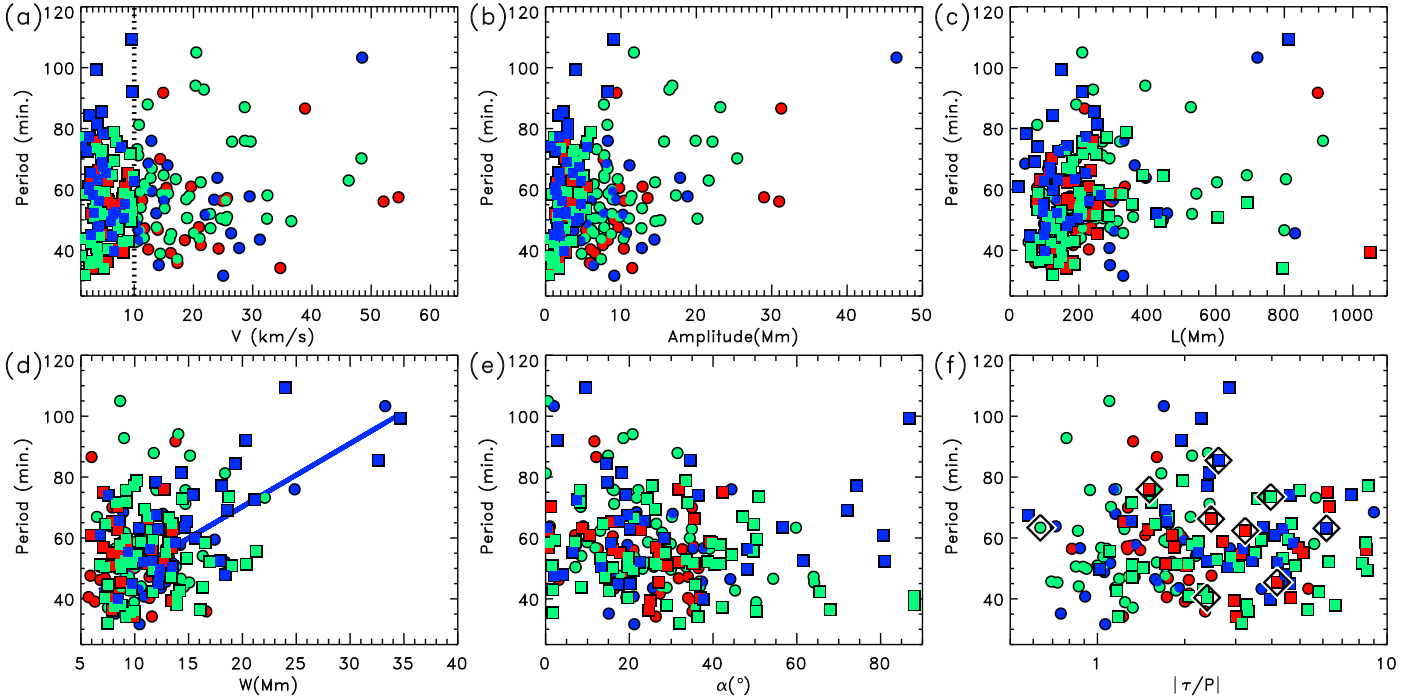


Figure 21. Scatter plots of period, P , vs. (a) velocity amplitude, V ; (b) displacement amplitude, A ; (c) length of the spine, L ; (d) width of the spine, W ; (e) angle between the direction of motion and the spine, α ; (f) damping time per period, $|\tau/P|$. The square symbols are for SAO events ($V < 10 \text{ km s}^{-1}$), and circles are for LAOs ($V \geq 10 \text{ km s}^{-1}$). For greater clarity, the error bars are not plotted, but can be found in Tables 1–8. The colors represent the filament type: active region (AR, red), intermediate (IT, green), and quiescent (QS, dark blue). The big black diamonds indicate events with negative values of τ/P .

10.4. Displacement, A

The maximum displacement of the filament mass with respect to the equilibrium position during the fitted oscillation, A , was derived from Equation (2):

$$A = \text{MAX}(|A_0 e^{-A_1(t-t_0)} \cos [A_2(t-t_0) + A_3]|). \quad (4)$$

The distributions of A for SAOs and LAOs differ substantially (Figure 26(a)). For SAOs, the distribution is concentrated at the origin with a large peak in the range 0–5 Mm, many fewer events between 5–10 Mm, and no events with $A > 10$ Mm. In contrast, LAO displacements cover a larger range ($A = 0$ –50 Mm), with a peak at 7.5 Mm. The A distributions for the three filament types are similar, with a maximum in the range 0–5 Mm and a decreasing number of events for increasing A (Figure 26(d)).

In the P – A scatter plot (Figure 21(b)), SAOs are concentrated at $A < 10$ Mm, while LAOs extend up to $A = 46$ Mm. Note that no events have large A and low P . Because the velocity amplitude is approximately $V \sim A/P$, the region of large A and low P corresponds to very large V values where no events were found in our survey. Recently we discovered an oscillation event with the largest velocity amplitude reported thus far (100 km s^{-1}) and a displacement of more than 50 Mm Luna et al. (2017), which would fit in the empty region of Figure 21(b).

In the A – α scatter plot (Figure 22(b)) we see that the range of displacements is reduced when α increases. Similar to the V – α or τ/P – α plots, A drops significantly for $\alpha > 40^\circ$ and there are no LAOs for $\alpha > 65^\circ$. This suggests that the oscillation or excitation mechanisms differ on either side of $\alpha = 40^\circ$, as discussed in Sections 10.1 and 10.3. Figure 23(c) shows that A is independent of the filament latitude.

10.5. Direction of Motion, α

Parameter α is the angle between the direction of the oscillation and the filament spine (Section 9). Within the catalog we found oscillations in any direction from 0° to 90° (Figure 26(b)). The total distribution has a peak close to 18° and a mean value of $27^\circ \pm 18^\circ$. For LAOs, the maximum is $\sim 28^\circ$ with a mean of $25^\circ \pm 14^\circ$, while for SAOs, the peak is also close to 18° and the mean value is $29^\circ \pm 21^\circ$. The number of events decreases for $\alpha > 40^\circ$, and only SAOs have $\alpha > 65^\circ$, as we found for the V – α , $|\tau/P|$ – α , and A – α scatter plots (Sections 10.1–10.4). Therefore, we define two populations of oscillations with respect to α : 163 events with $\alpha < 40^\circ$ and 33 with $\alpha > 40^\circ$.

Figure 26(b) shows that LAOs and SAOs have similar α distributions. The mean values are consistent with direct measurements of the angle between the filament magnetic field and its spine ($\alpha \sim 25^\circ$ on average; Leroy et al. 1983, 1984; Tandberg-Hanssen 1995; Trujillo Bueno et al. 2002; Casini et al. 2003; López Ariste et al. 2006). This suggests that most of the oscillations in the cataloged events are aligned with the magnetic field (longitudinal).

The α distribution is clearest for IT events (Figure 26(e)): the oscillations are aimed in all directions, but the peak coincides with the mean at $25^\circ \pm 13^\circ$. The α distribution for AR events has a peak at 37.5° with a mean value of $25^\circ \pm 14^\circ$. Interestingly, there are no oscillations in AR filaments with $\alpha > 45^\circ$, indicating that the motions are mainly longitudinal. For QS filaments, the distribution has a maximum around 18° and a mean value at $22^\circ \pm 20^\circ$. The QS α –distribution covers the entire domain, but the oscillation offsets are mainly below 40° . In summary, the mean α values for all filament types agree with the observed magnetic field orientation relative to the

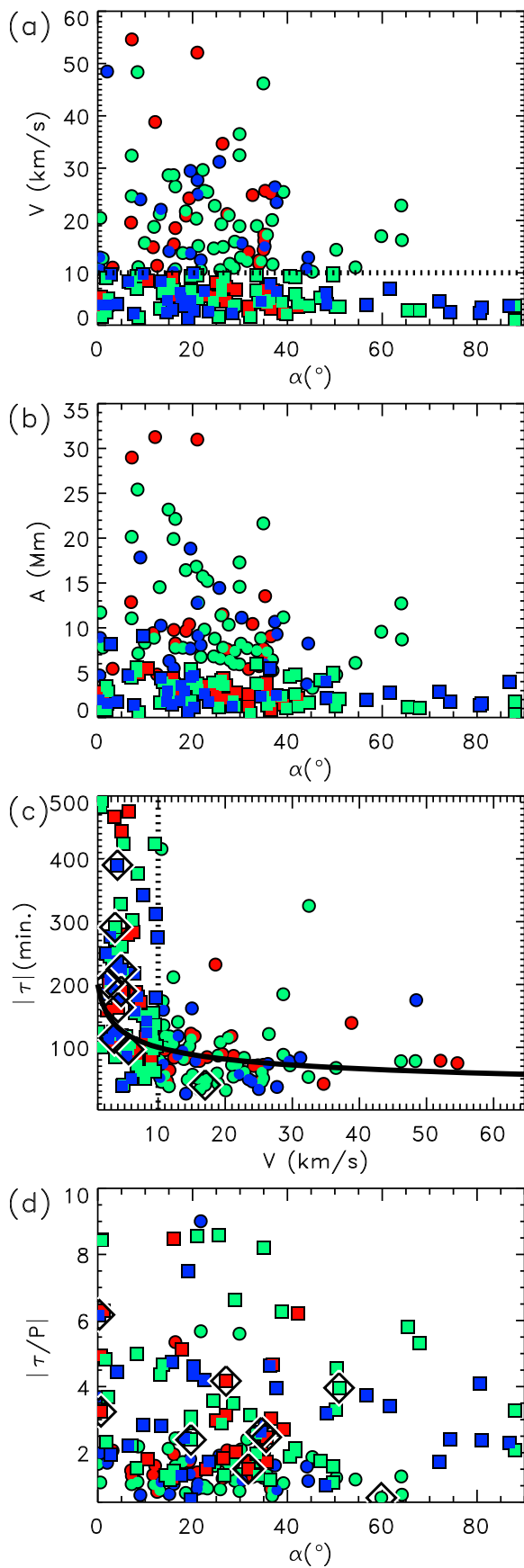


Figure 22. Scatter plots of (a) damping time, τ , vs. V ; (b) $|\tau/P|$ vs. α ; (c) V vs. α ; (d) A vs. α . Symbols and colors are as in Figure 21.

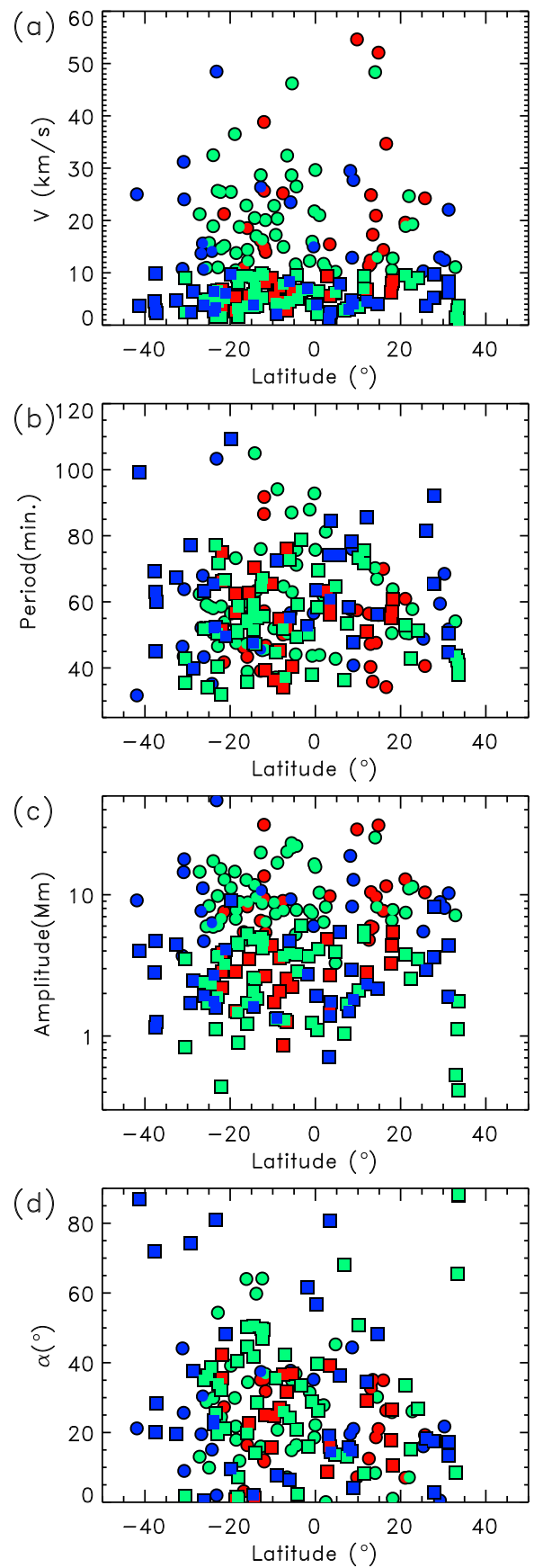


Figure 23. Scatter plots of latitude vs. (a) P ; (b) α ; (c) A ; (d) V . Symbols and colors are as in Figure 21.

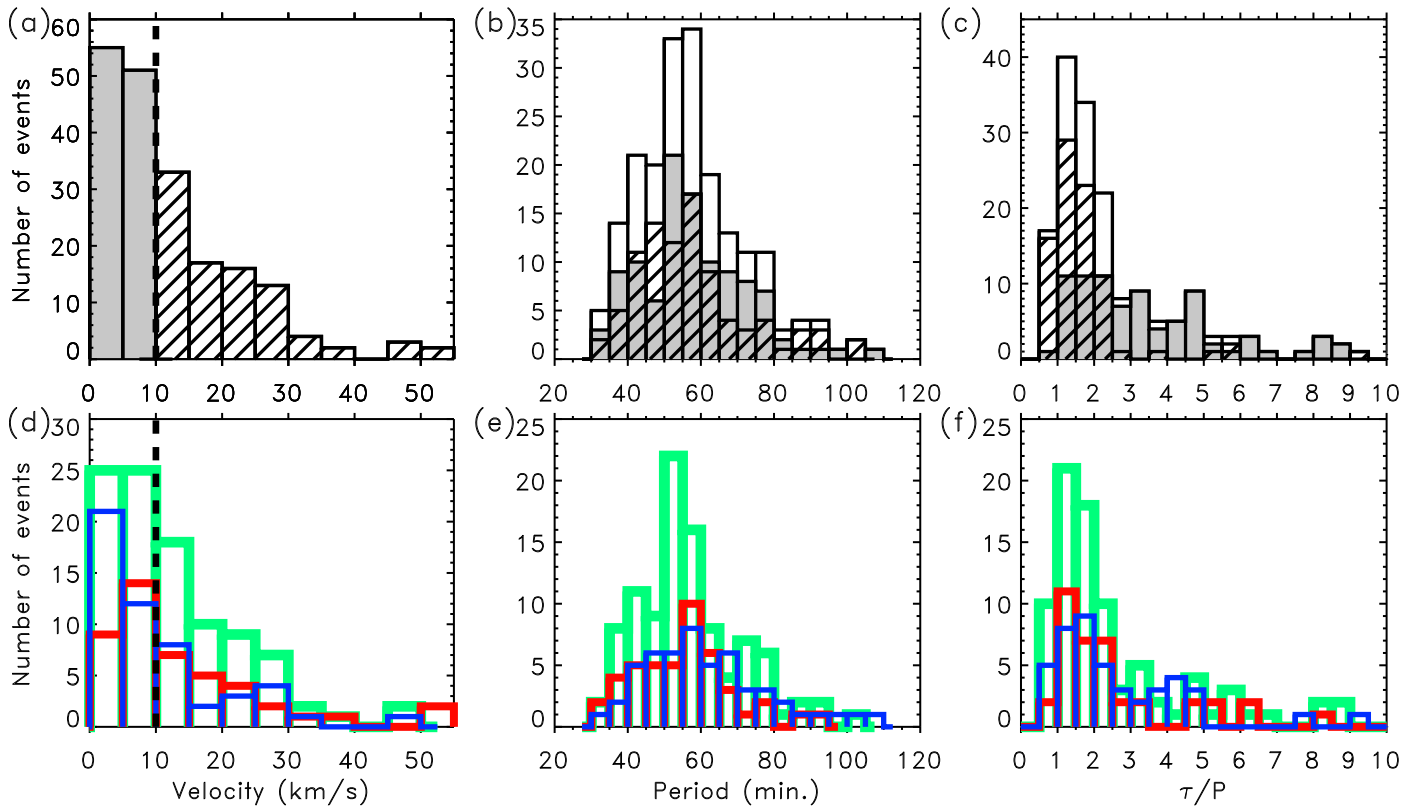


Figure 24. Histograms of the number of events binned by V (first column), P (second column), and $|\tau/P|$ (third column). In the top row, the shaded and striped areas represent SAO and LAO events, respectively, for three properties: V (a), P (b), and $|\tau/P|$ (c). In (a) the vertical dashed line indicates the separation between SAOs and LAOs at $V = 10 \text{ km s}^{-1}$. In (b) and (c) the curve with a white area underneath is the histogram of the total number of events. In the bottom row, histograms of (d) V , (e) P , and (f) $|\tau/P|$, divided according to the three types of filaments (active region [AR, red], intermediate [IT, green], and quiescent [QS, blue]), are shown.

spine, implying longitudinal polarization, particularly for IT filaments.

10.6. Latitude

Prominence oscillations may reflect the global structure of the supporting filament channels, which is intrinsically tied to the large-scale solar magnetic field. Figure 23 displays several oscillation properties— V , P , A , and α —as functions of solar latitude in Stonyhurst Heliographic Coordinates (Thompson 2006). V , P , and α generally display larger ranges of values at specific latitudes. For IT filaments, these oscillation properties largely occupy the region between -25° and 0° latitudes (see Figures 23(a)–(d)). In contrast, AR events exhibit larger ranges of these properties around two latitudes, -15° and 15° . For A this trend is less evident (Figure 23(c)), but a 2D histogram (not shown) reveals the same trend.

The latitude distribution (Figure 26(c)) shows that all survey events were located between 50° and -50° , typical for solar maximum. However, a substantial fraction of events accumulated around -15° , in the southern hemisphere, regardless of oscillation type (SAO or LAO). In Figure 26(f) the latitude distributions for the three filament types are shown. The distribution peaks at -15° and 15° for AR filaments, at -15° for IT filaments, and at -25° and 5° for QS filaments. It is evident from Figures 26(c) and (f) that the regions of a large number of events coincide with the regions of large dispersion of oscillation parameters of Figure 23. This suggests that in those latitudes, there are more filaments and more activity triggering oscillations. In this sense, the existence of these latitudes is not necessarily showing a latitudinal dependence of

oscillation parameters or intrinsic characteristics of the filaments.

Bashkirtsev & Mashnich (1993) found a smooth, sinusoidal latitudinal dependence for 30 SAO events observed over more than 8 years, with periods of 80 minutes at -20° and 20° latitudes and 40 minutes at 0° . We have not found a clear relationship between the periods or other properties and the filament latitude. Their study covered almost a solar cycle, so their latitudinal dependence could be related to the well-known migration of filaments from the poles toward the equator during the cycle. To determine whether this potentially profound relationship is solid, our catalog would have to be expanded significantly to include oscillation events throughout at least 1 solar cycle.

11. Seismology

Prominence seismology combines observations and theoretical modeling to infer hard-to-measure parameters such as the magnetic field (see Section 1). There are essentially three driving mechanisms for prominence oscillations: gravitational force, pressure imbalance, and magnetic Lorentz force.

Longitudinal oscillations are driven by a combination of gravity projected along the field (pendulum model; Luna & Karpen 2012) and gas pressure gradients (slow modes; Joarder & Roberts 1992). In the pendulum model, the period depends exclusively on the radius of curvature of the dips supporting the cool prominence plasma, R . Luna et al. (2012) and Zhang et al. (2013) determined that gas pressure gradients contribute negligibly to the restoring force when the radius of curvature is much smaller than a limit defined by the prominence

characteristics ($R \ll R_{\text{lim}}$), where R_{lim} is

$$R_{\text{lim}} = 1/4L_t(L_f - L_t) \kappa g/c_{\text{sc}}^2. \quad (5)$$

Here κ is the temperature contrast between the cool and adjacent hot plasmas, L_f is the field line length, L_t is the thread length, g is the solar gravitational constant, and c_{sc} is the coronal sound speed. In that case the period is

$$P = 2\pi\sqrt{\frac{R}{g}}. \quad (6)$$

Assuming that the magnetic tension in the dipped part of the tubes must be larger than the weight of the threads, the minimum magnetic field strength, B , depends on the particle number density of the prominence thread, n , and the period, P . In the absence of direct density measurements, Luna et al. (2014) adopted the range of typical values $n = 10^{10}\text{--}10^{11}\text{ cm}^{-3}$ as the main source of uncertainty and determined that

$$B(\text{G}) \geq (0.28 \pm 0.15) P(\text{minutes}). \quad (7)$$

For transverse horizontal oscillations, Kleczek & Kuperus (1969) assumed that the filament was supported by a single line-tied magnetic flux tube, and that the restoring force was supplied by magnetic tension. We assume again that n takes typical prominence values, and using their Equation (9), we find

$$B(\text{G}) = (5.5 \pm 3) \frac{L(\text{Mm})}{P(\text{minutes})}, \quad (8)$$

where L is the length of the filament. The uncertainty in the numerical coefficient is associated with the uncertainty in n .

Without additional data analysis and field extrapolation (e.g., Luna et al. 2017), it is difficult to establish which catalog events are oscillations parallel or perpendicular to the magnetic field. However, our statistical analysis revealed a clear distinction between oscillations with $\alpha < 40^\circ$ and those with $\alpha > 40^\circ$ (Section 10). Although the two populations are not necessarily uniquely associated with different oscillation polarizations, for seismology purposes we applied the longitudinal model to the oscillations with $\alpha < 40^\circ$ and the transverse model to the $\alpha > 40^\circ$ cases. This is also justified because the two models predict approximately the same B for a given event. We determined B and R from Equations (6) and (7) for the events with $\alpha < 40^\circ$ (Figure 27(a)). The shaded area covers the uncertainties in B . The magnetic field ranges from 9 to 48 G, and R from 25 to 300 Mm. The mean values are $B = 16$ G and $R = 89$ Mm. The obtained values are consistent with the rare direct measurements of prominence magnetic fields (see the review by Mackay et al. 2010).

The magnetic field plotted in Figure 27(a) is a lower limit, so we expect larger values to occur. In particular, the field could be significantly underestimated for small radii of curvature, R . The reason is that the magnetic tension is proportional to B^2/R and the weight of the prominence is proportional to $n g$. Thus, assuming similar n , the B necessary to balance the gravity is smaller for smaller R than for larger R .

In order to check the validity of the pendulum model, we computed Equation (5) and compared it with R for all catalog cases. Because we do not have direct measurements of L_f and L_t , we used L and W , the length of the spine and width of the filament. W is probably comparable to the thread lengths, but L is a lower limit on the length of the sheared field lines in the filament channel for $\alpha > 0$. c_{sc} is typically $\sim 200\text{ km s}^{-1}$, and

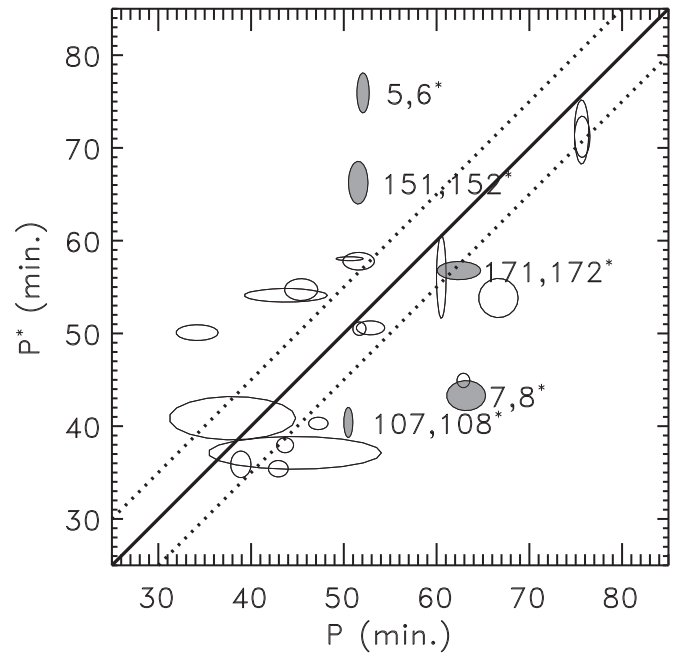


Figure 25. Scatter plot of the two periods in double events in the same filament. P is the first oscillation period, and P^* is the subsequent one. The data are shown as ellipses, where the vertical semi-axis is the error bar for P^* and the horizontal semi-axis is the error bar for P . Shaded ellipses are for double events including one amplified oscillation, with the relevant event numbers written on the side of each ellipse.

the typical temperature contrast is $\kappa = 100$. The resulting R_{lim} is largely greater than R_{lim} , demonstrating the applicability of the pendulum model to the catalog events.

Figure 27(b) shows the inferred magnetic field as a function of α . The pendulum model (Equation (7)) is used for events with $\alpha < 40^\circ$, and transverse model (Equation (8)) for $\alpha > 40^\circ$. For longitudinal oscillations ($\alpha < 40^\circ$), the B range generally decreases with α , reminiscent of the behavior of P . The same trend applies to the transverse oscillations ($\alpha > 40^\circ$), although some events reach large B values (38 G). For transverse oscillations, the B values are consistent with direct measurements (see, e.g., Harvey 1969). Our AR events are all longitudinal, while IT and QS events occupy both categories. It is interesting to note that the minimum field strengths do not differ significantly among the filament types, although AR filaments are embedded in higher field strength regions. This lower limit is consistent with direct measurements in AR filaments (Kuckein et al. 2009, 2012; Sasso et al. 2010, 2014), showing strong fields of up to several hundred Gauss.

12. Summary and Conclusions

In this work we have surveyed prominence oscillations detected through our visual inspection of the GONG network $H\alpha$ data during 2014 January–June, providing an extensive sample of events close to solar maximum of cycle 24. We have cataloged a large variety of oscillations including strongly damped motions, undamped oscillations, and amplified oscillations, enabling the first statistically significant study of filament oscillations and their pertinent properties. The filament and oscillation parameters are described in the text and tables; additional information and animations can be found in

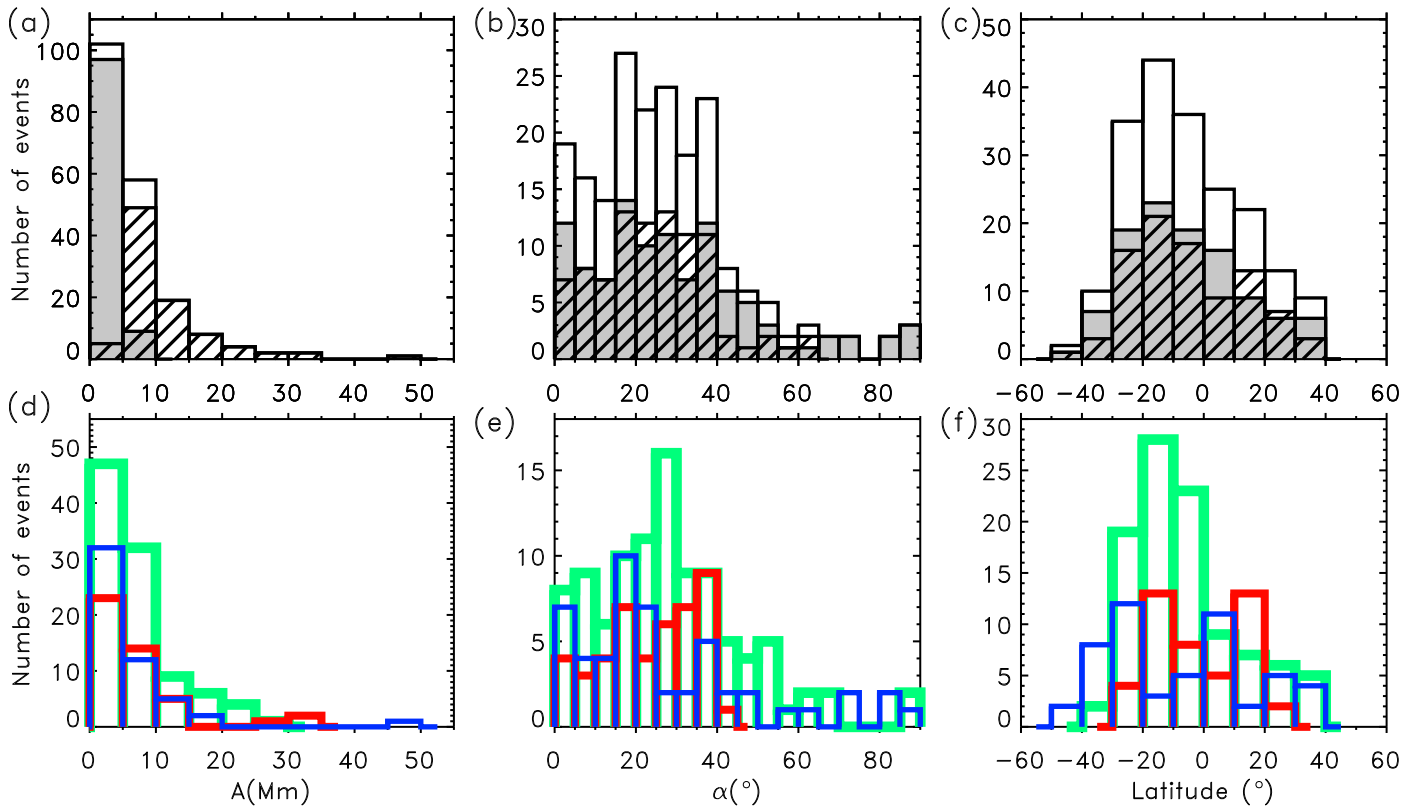


Figure 26. Histograms of the number of events binned by A (first column), α (second column), and latitude (third column). Panels and annotations are as in Figure 24.

the online catalog: <http://www.iac.es/galeria/mluna/pages/gong-catalogue-of-laos.php>.

We have found 196 oscillation events, including 106 SAOs and 90 LAOs. In 85 cases we have identified the triggering agents of the oscillations as flares, prominence eruption, jet, and a Moreton wave. For the remaining 111 events, the triggering agent is not identified. The occurrence rate of one LAO event every 2 days implies that LAOs are common phenomena on the Sun, as are SAOs.

We have parametrized the oscillations by fitting an exponentially decaying sinusoid, and statistically the distributions and correlations of key physical parameters. The fitted velocity amplitudes, V , are in the range $1.6\text{--}55\text{ km s}^{-1}$, and show a clear tendency to occur less frequently with increased V . This indicates that the LAOs are less common than SAOs, particularly since we probably underestimated the number of SAOs approaching the small-amplitude limit. The V range decreases with α , dropping sharply for events beyond 40° , and there are no LAOs for $\alpha > 65^\circ$.

The oscillation periods, P , range from 32 to 110 minutes. Surprisingly, the periods of both LAOs and SAOs have well-defined distributions centered at $P = 58 \pm 15$ minutes. This indicates that LAOs and SAOs are not two distinct populations of events with respect to their periods. For all three filament types, the mean oscillation period is around 1 hr. The P range decreases with the angle between the oscillation displacement and the filament spine, α . In general, we have not found strong correlations between P and other oscillation parameters.

The damping time per period, τ/P , covers a large range, including some cases with negative values (amplification). The τ/P distribution for LAOs peaks at 1.25, and most of the events exhibit very strong damping. For SAOs, the range of observed τ/P values is wider, peaking at 1.75. The three filament types

behave similarly. For LAOs, τ and τ/P decrease with V , regardless of filament type, confirming that LAOs involve nonlinear motions with velocity-dependent damping. This is a very interesting result because the kinetic energy involved in large-amplitude oscillations is enormous, due to the combination of large thread masses and large velocities. Therefore, the physical mechanism must be efficient enough to damp the substantial motion in a few oscillations. Our earlier theoretical studies showed that reasonable rates of mass accretion could explain the observed damping rates. On the other hand, the observed relation between τ and V is consistent with the Zhang et al. (2013) scaling law, $\tau \sim V^{-0.3}$, which suggests that the damping is associated with radiative cooling. More observational and theoretical work needs to be done to understand the damping process more thoroughly.

For the catalog events, the direction of the motion with respect to the filament spine, α , covers all possible angles between 0° and 90° , and the α distributions for LAOs and SAOs exhibit no clear peak. However, the mean α value is the same for all three filament types: 27° , which agrees with previous direct measurements of $\alpha \sim 25^\circ$ on average (Leroy et al. 1983, 1984; Tandberg-Hanssen 1995; Trujillo Bueno et al. 2002; Casini et al. 2003; López Ariste et al. 2006). Thus most of the oscillation displacements are probably aligned with the filament magnetic fields.

We have not found evidence of any relationships between the oscillation parameters and the solar latitude, in contrast to the findings of Bashkirtsev & Mashnich (1993). However, their study covered almost a solar cycle, and their latitudinal dependence could be associated with the well-known migration of filaments from poles to equator. To determine whether this profound relationship is solid, our catalog must be expanded to include events throughout at least 1 solar cycle.

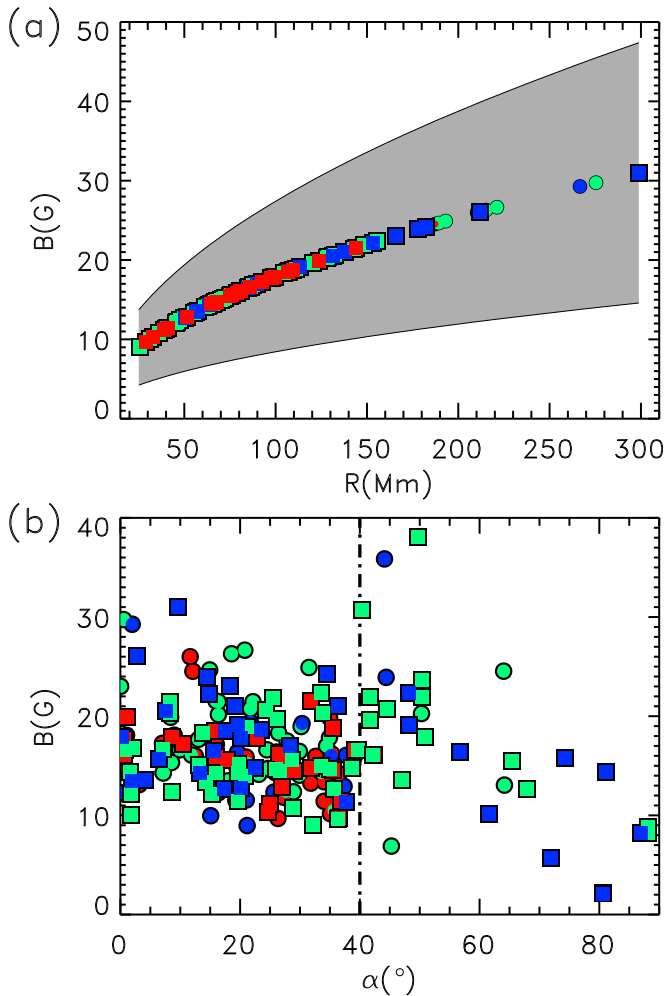


Figure 27. Seismology diagnostics for longitudinal and transverse oscillations. (a) The lower limit on B as a function of R for longitudinal oscillations. The shaded area corresponds to the uncertainty range. (b) The estimated magnetic field strength for events with longitudinal and transverse oscillations, from Equations (7) and (8), respectively. The vertical dot-dashed line indicates the assumed separation between longitudinal and transverse oscillations. Symbols and colors are as in the scatter plots.

We have applied seismological techniques to the entire catalog. For the longitudinally oscillating cases, we determined the radius of curvature of the magnetic dips hosting the prominence, R , and the minimum field strength, B , required to support the mass against gravity. $R = 25\text{--}300$ Mm and $B = 2\text{--}38$ G, with mean values of $R = 89$ Mm and $B = 17$ G. For transverse oscillations, the magnetic field strength derived from the magnetic restoring force yields a wider range of $B = 2\text{--}38$ G but a similar mean value.

Most of the oscillations are longitudinal, with the motion directed along the local magnetic field. Surprisingly, the period distributions for both SAOs and LAOs have a strong peak centered at 58 minutes, which implies that most solar filaments share a common structure. Namely, their structure is composed of dipped flux tubes with a radius of curvature of ~ 90 Mm and an angle between the threads and the spine of $\sim 30^\circ$. The magnetic field strength is probably larger than the minimum estimate of 16 G. We also found that many SAOs are initiated by energetic disturbances, which contradicts the idea that SAOs are exclusively driven by photospheric or chromospheric waves. On the other hand, Ning et al. (2009)

and Hillier et al. (2013) studied numerous oscillations in small prominence features, and found velocities in general below 10 km s^{-1} and periods of the order of minutes. These localized versions of SAOs are more consistent with wave driving than our SAOs, which affect large portions or the entire filament.

In future research we will extend the catalog to events near the solar minimum of the same cycle 24, to augment our statistics and explore the possibility that oscillation parameters and filament properties evolve during the solar cycle. We invite the community to utilize this catalog for other research projects and to aid in expanding its contents, in order to advance our understanding of the fundamental structure and evolution of solar prominences.

The Global Oscillation Network Group (GONG) Program is managed by the NSO and operated by AURA, Inc., under a cooperative agreement with the NSF. The data are acquired by instruments operated by the Big Bear Solar Observatory, High Altitude Observatory, Learmonth Solar Observatory, Udaipur Solar Observatory, Instituto de Astrofísica de Canarias, and Cerro Tololo Interamerican Observatory. The operation of Big Bear Solar Observatory is supported by NJIT, US NSF AGS-1250818, and NASA NNX13AG14G grants. This paper made use of the IAC Supercomputing facility HTCondor (<http://research.cs.wisc.edu/htcondor/>), partly financed by the Ministry of Economy and Competitiveness with FEDER funds, code IACA13-3E-2493. This research also made use of NASA Astrophysics Data System.

This work was initiated during International Space Science Institute (ISSI) team 314 meetings in Bern, led by M. Luna, on “Large-amplitude Oscillations in Solar Prominences.” M. Luna acknowledges the support by the Spanish Ministry of Economy and Competitiveness through project AYA2014-55078-P. H. Gilbert, J. Karpen, T. Kucera, and K. Muglach acknowledge support by the NASA Heliophysics Guest Investigator program. K. Muglach also acknowledges NASA cooperative agreement NNG11PL10A. J. Terradas and J. L. Ballester want to thank the financial support from MINECO AYA2014-54485-P and FEDER Funds, and the Conselleria d’Innovació Recerca i Turisme del Govern Balear to IAC3.

Appendix Time–Distance Diagrams in Curved Slits

The GONG network telescopes offer fairly good spatial resolution of around 1 arcsec per pixel. However, the seeing conditions at the network telescope locations often limit the quality of the images, yielding poor effective spatial resolution greater than 1 arcsec. As we discussed in Section 2, it was necessary to follow the motion of the large-amplitude displacements with curved paths in order to accurately track the entire motion of the filament.

A time–distance diagram is constructed to follow the motion along the path defined by the artificial slit. In many cases (e.g., Luna et al. 2014), straight slits consisting of rectangles of length l and width w in pixels are placed lengthwise along the path of the motion studied. In order to increase the signal-to-noise ratio, the intensity is averaged along the width w , which essentially projects the intensity onto the axis of the slit. The resulting intensity along the slit as a function of time is the time–distance diagram. Using a curved slit is theoretically similar to using a straight slit. In a

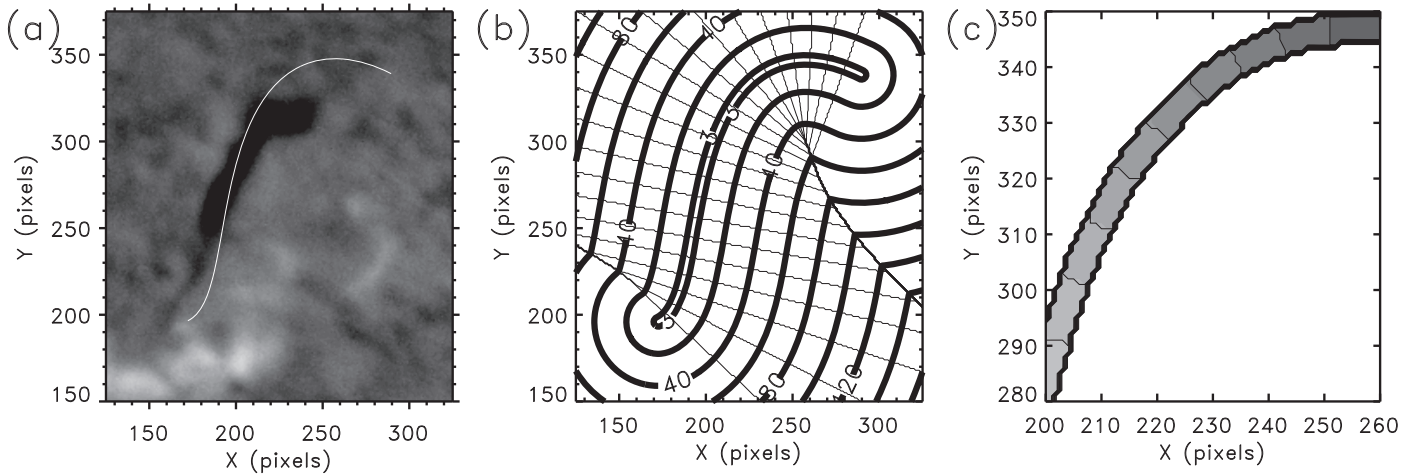


Figure 28. (a) $H\alpha$ image of case 1. The filament is located in the center of the image. The white curve is the axis of the slit, S . (b) Isocontours of $\text{Dist}(i, j)$ and $\text{Int}(i, j)$ (Equation (9)) for the image in (a). (c) Close-up view of a region of the slit showing the bins used to construct the time–distance diagram. All positions inside the bins have $B(i, j) = q = \text{constant}$ (Equation (11)). The gray gradient highlights the different bins, with white corresponding to $q = 1$ and black to $q = N_{\text{pix}}$.

curved slit, the projection is defined along the normal lines to the curved slit axis. Thus, for each pixel, there is a normal line intersecting the slit axis at (x_q, y_q) , and the distance between the pixel and the slit is d (i.e., between the pixel and (x_q, y_q)). A pixel belongs to the slit if $d \leq w/2$.

In general, an image is described by the 2D function $I(x, y)$, where I is the intensity in the filter considered ($H\alpha$ in our situation) and x and y are the coordinates of each position in the image. We assume, without loss of generality, that the origin of the coordinates $(x, y) = (0, 0)$ is at the left-bottom boundary of the image. These coordinates are integer multiples of the resolution δ of the image; then $x = i\delta$ and $y = j\delta$, where i and j define the position within the image in pixels. Alternatively, the image can be described in pixels $I(i, j)$.

We first define a sufficiently smooth curve, S , that represents the axis of the slit, by clicking repetitively on the image along the path of the oscillatory motion and fitting these points with a fourth degree polynomial function. The white line in Figure 28(a) shows the curve S obtained for event 1 of the catalog. We divide this curve into segments of length δ in order to pixelate the curve as the image. The coordinate along the slit axis is then $s = \delta q$, where q is a one-dimensional array with $N_{\text{pix}} = l/\delta$ elements.

The time–distance diagram consists of $I(t, i_q, j_q) = \langle I(t, A) \rangle$, where (i_q, j_q) is the position of the q -segment of the axis of the slit, t is time, A is an area surrounding (i_q, j_q) , and $\langle \dots \rangle$ indicates the average of the intensity over A . The main difficulty is how A is defined. Some authors just define a square area centered at (i_q, j_q) . However, this mixes the intensities from points that are not projected perpendicularly to the slit, and some pixels are projected twice in consecutive segments of the slit. We will define A as the area enclosed by the normal lines between both ends of the slit segment, q , and within the slit, $d \leq w/2$.

For this end, we define two matrices: $\text{Dist}(i, j)$ is the distance from any point (i, j) to the closest point along the slit, and $\text{Ind}(i, j)$ is the index of that point along the slit. These are

$$\text{Dist}(i, j) = \text{MIN} \left(\frac{1}{\delta} \sqrt{(x_i - x_q)^2 + (y_j - y_q)^2} \right) \quad (9)$$

$$\text{Ind}(i, j) = q_{\text{min}}, \quad (10)$$

where the MIN is the minimum over the q index. We construct these arrays by computing the distance $\sqrt{(x_i - x_q)^2 + (y_j - y_q)^2}$ between each pixel of the image (i, j) and all the positions over the slit, q . This is equivalent to computing the distance, d , between the pixel and the slit axis. However, this way is much more computationally effective. To calculate $\text{Ind}(i, j)$, we then find the value of q_{min} that minimizes the distance $\sqrt{(x_i - x_q)^2 + (y_j - y_q)^2}$. This is the position over the slit where the intensity of the image pixel will be projected. We repeat this process for all image pixels and obtain the arrays defined by Equations (9) and (10). Thus $\text{Dist}(i, j)$ is the distance measured in pixels from (i, j) to the curve S . The closed thick lines in Figure 28(b) are the isolines of the Dist function over the image. We see that each isoline represents the positions of the pixels that are equidistant to the curve segment S (i.e., the slit axis). In the example of Figure 28, the slit has $w = 6$, which corresponds to the area inside the most internal isoline with a distance to S of 3 pixels. In general, we define the slit as the set of pixels (i, j) that fulfills the condition $\text{Dist}(i, j) \leq w/2$. Thus, to select the pixels inside the slit, we define a masking function

$$\text{Mask}(i, j) = \begin{cases} 1, & \text{if } \text{Dist}(i, j) \leq w/2 \\ 0, & \text{if } \text{Dist}(i, j) > w/2. \end{cases} \quad (11)$$

The thin straight lines in Figure 28(b) plot the isolines of the Ind matrix. This isolines coincide with the normal lines to the slit axis. We define a new function,

$$B(i, j) = \text{Mask}(i, j) \times \text{Ind}(i, j). \quad (12)$$

The values in this array are zero outside the slit and range from 1 to N_{pix} in the slit. In this way we have binned the regions of the image that are going to be averaged over the q -position of the slit. We clearly see these bins of constant $B(i, j)$ in Figure 28(c), as well as the bins defined by the area inside the region formed by the isolines of Dist and Int . Then the intensity over the slit, $I(q)$, is the average of the intensity over the bin, where $B(i, j) = q$ —that is,

$$I(q) = \langle I(B(i, j) = q) \rangle. \quad (13)$$

This technique can also be used for straight slits to reduce the computational time, because the images do not need to be rotated in order to align the x - or y -axis with the direction of the slit. Repeating this procedure for each image within the temporal sequence, we obtain the time–distance diagram, $I(t, q)$.

One problem with this technique is that the function Ind is multivalued in some regions (i.e., one pixel is equidistant to several points within the slit). These problematic regions are located at the intersections of the isolines of Ind . Figure 28(b) reveals two lines of multivalued points that coincide with the center of curvature of one segment of the slit. However, we avoid these regions by selecting sufficiently smooth curves with the center of curvature outside the slit area.

ORCID iDs

M. Luna  <https://orcid.org/0000-0002-3841-313X>
 J. Karpen  <https://orcid.org/0000-0002-6975-5642>
 J. L. Ballester  <https://orcid.org/0000-0001-8921-9225>
 J. Terradas  <https://orcid.org/0000-0002-7013-1933>
 T. Kucera  <https://orcid.org/0000-0001-9632-447X>

References

- Arregui, I., Ballester, J., & Goossens, M. 2008a, *ApJL*, 676, L77
 Arregui, I., Oliver, R., & Ballester, J. L. 2012, *LRSP*, 9, 2
 Arregui, I., Terradas, J., Oliver, R., & Ballester, J. 2008b, *ApJL*, 682, L141
 Asai, A., Ishii, T. T., Isobe, H., et al. 2012, *ApJL*, 745, L18
 Ballester, J. L., Carbonell, M., Soler, R., & Terradas, J. 2016, *A&A*, 591, A109
 Balthasar, H., Wiehr, E., Schleicher, H., & Wöhl, H. 1993, *A&A*, 277, 635
 Bashkirtsev, V. S., & Mashnick, G. P. 1993, *A&A*, 279, 610
 Becker, U. 1958, *ZA*, 44, 243
 Bi, Y., Jiang, Y., Yang, J., et al. 2014, *ApJ*, 790, 100
 Bocchialini, K., Baudin, F., Koutchmy, S., Pouget, G., & Solomon, J. 2011, *A&A*, 533, A96
 Bruzek, A. 1951, *ZA*, 28, 277
 Bruzek, A., & Becker, U. 1957, *ZA*, 42, 76
 Casini, R., López Ariste, A., Tomczyk, S., & Lites, B. W. 2003, *ApJL*, 598, L67
 Chen, P., Innes, D., & Solanki, S. 2008, *A&A*, 484, 487
 Dodson, H. W. 1949, *ApJ*, 110, 382
 Dyson, F. 1930, *MNRAS*, 91, 239
 Efremov, V. I., Parfinenko, L. D., & Solov'ev, A. A. 2016, *SoPh*, 291, 3357
 Engvold, O. 2015, in *Solar Prominences*, Astrophysics and Space Science Library, Vol. 415, ed. J.-C. Vial & O. Engvold (Cham: Springer International), 31
 Eto, S., Isobe, H., Narukage, N., et al. 2002, *PASJ*, 54, 481
 Foullon, C., Verwichte, E., & Nakariakov, V. M. 2004, *A&A*, 427, L5
 Foullon, C., Verwichte, E., & Nakariakov, V. M. 2009, *ApJ*, 700, 1658
 Gilbert, H. R., Daou, A. G., Young, D., Tripathi, D., & Alexander, D. 2008, *ApJ*, 685, 629
 Gosain, S., & Foullon, C. 2012, *ApJ*, 761, 103
 Harvey, J. W. 1969, PhD thesis, Univ. Colorado, Boulder
 Harvey, J. W., Hill, F., Hubbard, R. P., et al. 1996, *Sci*, 272, 1284
 Hershaw, J., Foullon, C., Nakariakov, V. M., & Verwichte, E. 2011, *A&A*, 531, A53
 Hillier, A., Morton, R. J., & Erdelyi, R. 2013, *ApJL*, 779, L16
 Hyder, C. L. 1966, *ZAp*, 63, 78
 Isobe, H., & Tripathi, D. 2006, *A&A*, 449, L17
 Isobe, H., Tripathi, D., Asai, A., & Jain, R. 2007, *SoPh*, 246, 89
 Jing, J., Lee, J., Spirock, T. J., et al. 2003, *ApJL*, 584, L103
 Jing, J., Lee, J., Spirock, T. J., & Wang, H. 2006, *SoPh*, 236, 97
 Joarder, P. S., & Roberts, B. 1992, *A&A*, 261, 625
 Kleczek, J., & Kuperus, M. 1969, *SoPh*, 6, 72
 Kuckein, C., Centeno, R., Martínez Pillet, V., et al. 2009, *A&A*, 501, 1113
 Kuckein, C., Martínez Pillet, V., & Centeno, R. 2012, *A&A*, 539, A131
 Lemen, J. R., Title, A. M., Akin, D. J., et al. 2012, *SoPh*, 275, 17
 Leroy, J. L., Bommier, V., & Sahal-Brechot, S. 1983, *SoPh*, 83, 135
 Leroy, J. L., Bommier, V., & Sahal-Brechot, S. 1984, *A&A*, 131, 33
 Li, T., & Zhang, J. 2012, *ApJL*, 760, L10
 Lin, Y., Engvold, O., der Voort, L. R. v., Wiik, J. E., & Berger, T. E. 2005, *SoPh*, 226, 239
 Liu, W., Berger, T. E., & Low, B. C. 2012, *ApJL*, 745, L21
 López Ariste, A., Aulanier, G., Schmieder, B., & Sainz Dalda, A. 2006, *A&A*, 456, 725
 Luna, M., Díaz, A. J., & Karpen, J. 2012, *ApJ*, 757, 98
 Luna, M., & Karpen, J. 2012, *ApJL*, 750, L1
 Luna, M., Knizhnik, K., Muglach, K., et al. 2014, *ApJ*, 785, 79
 Luna, M., Su, Y., Schmieder, B., Chandra, R., & Kucera, T. A. 2017, *ApJ*, 850, 143
 Luna, M., Terradas, J., Khomenko, E., Collados, M., & Vicente, A. d. 2016, *ApJ*, 817, 157
 Luna, M., Terradas, J., Oliver, R., & Ballester, J. L. 2006, *A&A*, 457, 1071
 Luna, M., Terradas, J., Oliver, R., & Ballester, J. L. 2008, *ApJ*, 676, 717
 Mackay, D. H., Karpen, J. T., Ballester, J. L., Schmieder, B., & Aulanier, G. 2010, *SSRv*, 151, 333
 Molowny-Horas, R., Wiehr, E., Balthasar, H., Oliver, R., & Ballester, J. L. 1999, *JOSO Annu. Rep.*, 126
 Moreton, G. E., & Ramsey, H. E. 1960, *PASP*, 72, 357
 Neter, J., Wasserman, W., & Whitmore, G. 1993, *Applied Statistics* (Boston, MA: Allyn and Bacon)
 Newton, H. W. 1935, *MNRAS*, 95, 650
 Ning, Z., Cao, W., Okamoto, T. J., Ichimoto, K., & Qu, Z. Q. 2009, *A&A*, 499, 595
 Ofman, L., & Aschwanden, M. 2002, *ApJL*, 576, L153
 Okamoto, T. J., Nakai, H., Keiyama, A., et al. 2004, *ApJ*, 608, 1124
 Oliver, R. 1999, *ESA*, 448, 425
 Oliver, R., & Ballester, J. L. 2002, *SoPh*, 206, 45
 Pouget, G. 2007, PhD thesis, Université de Paris-Sud, Paris
 Pouget, G., Bocchialini, K., & Solomon, J. 2006, *A&A*, 450, 1189
 Ramsey, H. E., & Smith, S. F. 1966, *AJ*, 71, 197
 Ruderman, M., & Roberts, B. 2002, *ApJ*, 577, 475
 Ruderman, M. S., & Luna, M. 2016, *A&A*, 591, A131
 Sasso, C., Lagg, A., & Solanki, S. K. 2010, *A&A*, 526, A42
 Sasso, C., Lagg, A., & Solanki, S. K. 2014, *A&A*, 561, A98
 Shen, Y., Ichimoto, K., Ishii, T. T., et al. 2014a, *ApJ*, 786, 151
 Shen, Y., Liu, Y. D., Chen, P. F., & Ichimoto, K. 2014b, *ApJ*, 795, 130
 Takahashi, T., Asai, A., & Shibata, K. 2015, *ApJ*, 801, 37
 Tandberg-Hanssen, E. 1995, *The Nature of Solar Prominences*, Vol. 199 (Dordrecht: Kluwer)
 Terradas, J., Soler, R., Díaz, A. J., Oliver, R., & Ballester, J. L. 2013, *ApJ*, 778, 49
 Terradas, J., Soler, R., Luna, M., et al. 2016, *ApJ*, 820, 125
 Terradas, J., Soler, R., Luna, M., Oliver, R., & Ballester, J. L. 2015, *ApJ*, 799, 94
 Thompson, W. T. 2006, *A&A*, 449, 791
 Tripathi, D., Isobe, H., & Jain, R. 2009, *SSRv*, 149, 283
 Trujillo Bueno, J., Landi Degl'Innocenti, E., Collados, M., Merenda, L., & Manso Sainz, R. 2002, *Natur*, 415, 403
 Vršnak, B. 1993, *HvaOB*, 17, 23
 Vršnak, B., Veronig, A. M., Thalmann, J. K., & Žic, T. 2007, *A&A*, 471, 295
 Wang, B., Chen, Y., Fu, J., et al. 2016, *ApJL*, 827, L33
 Xue, Z. K., Yan, X. L., Qu, Z. Q., & Zhao, L. 2014, in *ASP Conf. Ser.* 489, *Solar Polarization 7*, ed. K. N. Nagendra et al. (San Francisco, CA: ASP), 53
 Zhang, Q., Li, D., & Ning, Z. 2017a, arXiv:1711.00670
 Zhang, Q. M., Chen, P. F., Xia, C., & Keppens, R. 2012, *A&A*, 542, A52
 Zhang, Q. M., Chen, P. F., Xia, C., Keppens, R., & Ji, H. S. 2013, *A&A*, 554, A124
 Zhang, Q. M., Li, T., Zheng, R. S., Su, Y. N., & Ji, H. S. 2017b, *ApJ*, 842, 27
 Zhou, Y.-H., Zhang, L.-Y., Ouyang, Y., Chen, P. F., & Fang, C. 2017, *ApJ*, 839, 9